Experimental Analysis of the Performance of a Wind-Turbine Airfoil Using Temperature-Sensitive Paint

Marco Costantini[1], Carsten Fuchs[2], Ulrich Henne[3], and Christian Klein[4],
Institute of Aerodynamics and Flow Technology, German Aerospace Center (DLR), D-37073 Göttingen, Germany

Vladimír Ondruš[5],
FH Münster - University of Applied Sciences, D-48565 Steinfurt, Germany

Martin Bruse[6], Markus Löhr[7], and Markus Jacobs[8]
The German-Dutch Wind Tunnels (DNW), D-37073 Göttingen, Germany

DOI https://doi.org/10.2514/1.J060039

Knowledge on the boundary-layer transition location at large chord Reynolds numbers is essential to evaluate the performance of airfoils designed for modern wind-turbine rotor blades. In the present work, a temperature-sensitive paint was used to systematically study boundary-layer transition on the suction side of a DU 91-W2-250 airfoil. The experiments were performed in the High-Pressure Wind Tunnel Göttingen at chord Reynolds numbers up to 12 million and angles-of-attack from -14° to 20°. The coefficients of airfoil lift, drag, and pitching moment were also obtained after integration of the pressure distributions measured on the surface and in the wake of the wind-tunnel model. The global information obtained via temperature-sensitive paint not only enabled the analysis of the change in the transition location with varying angle-of-attack and chord Reynolds number, but also provided an explanation for the evolution of the aerodynamic coefficients measured at stall and post-stall conditions. The stability of the laminar boundary layers investigated in the experiments was analyzed according to linear stability theory. The results of the stability

[1] Research Scientist, Department of Experimental Methods, Marco.Costantini@dlr.de (Corresponding Author)
[2] Technician, Department of Experimental Methods, Carsten.Fuchs@dlr.de
[3] Research Scientist, Department of Experimental Methods, Ulrich.Henne@dlr.de
[4] Research Scientist, Department of Experimental Methods, Christian.Klein@dlr.de, AIAA Associate Fellow
[5] Research Scientist, Department of Chemical Engineering, vlondrus@fh-muenster.de
[6] Head Data and Measurement Group, Business Unit BGK, Martin.Bruse@dnw.aero
[7] Technician, Business Unit BGK, Markus.Loehr@dlr.de
[8] Chief Aerodynamicist, Business Unit BGK, Markus.Jacobs@dlr.de

This article is based on the AIAA Paper No. 2019-0800, presented at the AIAA SciTech 2019 Forum, held on January 7-11, 2019, in San Diego, CA.

computations supported the experimentally observed variations in the transition location. The amplification factors of boundary-layer disturbances at transition were also determined by correlating the experimental and numerical results.

Nomenclature

AoA	=	angle-of-attack, ° or deg
b	=	wing span, m
c	=	chord length, m
c_D	=	drag coefficient
c_f	=	friction coefficient
c_L	=	lift coefficient
c_m	=	pitching moment coefficient
c_p	=	pressure coefficient
M	=	Mach number, based on freestream velocity and freestream speed of sound
N	=	natural logarithm of amplification ratio
p_0	=	total pressure, MPa
R_a	=	average roughness, µm
R_z	=	mean roughness depth, µm
Re	=	Reynolds number, based on chord length, freestream velocity and freestream kinematic viscosity
Tu	=	turbulence level
U_∞	=	freestream velocity, m/s
x	=	chordwise coordinate, positive downstream starting from the model leading edge, m
y	=	spanwise coordinate, positive starting from the model port side to the model starboard side, m
z	=	normal coordinate, positive upwards, m
Δ	=	difference
δ_1	=	boundary-layer displacement thickness, µm
λ	=	wavelength, nm
ν_∞	=	freestream kinematic viscosity, m^2/s

subscripts:

em = emission

ex = excitation

max = maximal value

s = separation

T = transition

I. Introduction

Wind energy is nowadays a significant source of energy. Taking as an example the European Union (EU), wind energy covered 16 % of the overall EU electricity demand in 2020 [1]. EU countries have agreed to cut greenhouse gas emissions by 80-95 % through 2050 [2], and one intermediate step to achieve this goal is to cover at least 27 % of EU energy demand via renewable energy by 2030 [3]. The contribution of wind energy to cover EU total power demand in 2030 is expected to be between 22 % and 36 %, depending on the scenarios predicted by a recent analysis of market and policy developments [4]. As a further example, similar scenarios have been considered also for the United States of America [5]. A large number of wind turbines will be installed to meet these targets. Optimizing performance would reduce the number of wind turbines installed to meet these targets at lower costs, or would even encourage additional installations to exceed these targets. Rotor-blade aerodynamics has an essential role in overall wind-turbine performance [6,7] and has continuously improved in the last decades. In the past, NACA airfoils were commonly used for wind-turbine blade sections, but in recent years aerodynamic research has developed airfoil classes dedicated to wind-turbine rotor blades [8]. Moreover, the size and shape of the airfoil varies depending on the spanwise section, with thick airfoils (maximal thickness larger than 28-30 % of the airfoil chord length c [9]) mounted at the inboard sections to satisfy structural demands and provide high lift, and airfoils with relatively small thickness (less than approx. 20 % c) used at the outboard sections to achieve large lift-to-drag ratios. In the mid-span area, airfoils with a thickness of about 25 % c are typically installed. They provide a compromise between the aerodynamic characteristics of airfoils used for outboard and inboard sections [8]. The airfoils for mid-span and outboard sections, however, are also subjected to Reynolds number and roughness effects [8,10-11]; both these effects are related to the occurrence of boundary-layer transition on the airfoils under practical conditions, and in particular on the extent of the laminar flow region. In fact, transition occurring upstream

of the design location leads to significantly larger drag [12], smaller lift and thus also to a smaller lift-to-drag ratio [10,13]. It is therefore crucial to design airfoils for mid-span and outboard sections that present low sensitivity to roughness [8,10,13] and to experimentally verify their performance at Reynolds numbers relevant for modern wind turbines with large rotor diameters (which can be of the order of 100 m). Especially in the mid-span area, the Reynolds number based on the airfoil chord $\mathrm{Re} = U_\infty c/\nu_\infty$ (where U_∞ and ν_∞ are the freestream velocity and kinematic viscosity, respectively) can be as large as $25 \cdot 10^6$ [14]. However, the maximal Reynolds number achievable in conventional wind tunnels is typically below $6 \cdot 10^6$ [13]. As an alternative to real-scale field experiments, a further increase of the Reynolds number test range in wind tunnels (while maintaining the Mach number low, i.e., at $M < 0.2$ [5]) can be obtained in two ways: by decreasing the gas temperature (and thus decreasing the gas dynamic viscosity and increasing the gas density), as in the case of cryogenic wind tunnels such as the Cryogenic Wind Tunnel Cologne (DNW-KKK) [14-17]; or by increasing the gas pressure (and thus the gas density), as done previously in the NASA Low Turbulence Pressure Tunnel (demolished in 2014) [18] and currently in the High Pressure Wind Tunnel Göttingen (DNW-HDG) [17,19-24]. This enables the study of the aerodynamic performance of airfoils developed for modern wind-turbine rotor blades in the appropriate Reynolds number range, thus avoiding the influence of a Reynolds number different from that achieved in practical applications.

Aerodynamic performance is typically examined in wind tunnels by measuring aerodynamic loads (either directly, by means of a strain gauge balance, or indirectly, by means of pressure measurements on the surface and in the wake of the wind-tunnel models) [5,8,10,13-15,21-23]. In general, these measurements do not provide any information (if any, only indirectly) on the airfoil / blade boundary-layer state and on boundary-layer transition, which is however essential for the evaluation and further improvement of the aerodynamic performance of wind-turbine rotor blades. This information can be provided by one or more rows of sensors, such as unsteady pressure sensors [15,25-26] or hot films [11,27], which however have intrinsically low spatial resolution, and can introduce significant disturbances into the thin boundary layer developing on the wind-tunnel model surface at large Reynolds numbers. Global, non-intrusive transition measurements can be carried out by means of thermographic methods, such as infra-red (IR) thermography [11,14,26,28] and the temperature-sensitive paint (TSP) technique [17,20,29-30]. IR thermography is widely used for transition detection at ambient conditions in conventional wind tunnels, and it has been successfully applied also in flight [28] and field experiments [26]; however, IR thermography cannot be applied easily at the cryogenic temperatures or at the high pressures needed to match the large Reynolds numbers of real wind-turbine rotor blades in wind tunnels [20,29]. Under these test conditions, boundary-layer transition can be successfully

measured by means of TSP [14,17,20].

In the present work, the aerodynamic performance of an airfoil designed for the mid-span region of modern wind-turbine rotor blades was experimentally investigated at large chord Reynolds numbers (up to $Re = 12 \cdot 10^6$) and low Mach numbers ($M < 0.1$) in the DNW-HDG wind tunnel. Because of its above-discussed importance for modern wind turbines, a main objective of this work was the study of the evolution of boundary-layer transition over a wide range of airfoil angles-of-attack (from -14° to 20°) for Reynolds numbers larger than those commonly found in the literature. Laminar-turbulent transition was measured globally by means of TSP, whereas the coefficients of airfoil lift, drag, and pitching moment were obtained after integration of the pressure distributions measured on the wind-tunnel model surface and in the model wake. The model surface pressure distributions served also as an input for boundary-layer computations, and the calculated boundary-layer velocity profiles were analyzed according to linear stability theory [12,31]. The results of the numerical analysis were then correlated with the transition locations measured in the experiments.

II. Experimental Setup

The experiments were conducted in DNW-HDG [19-24], a closed-return wind tunnel where air can be pressurized up to 10 MPa, thus allowing for Reynolds numbers up to approx. $20 \cdot 10^6$, based on the maximally achievable freestream velocity of $U_\infty = 38$ m/s and a typical model chord length $c = 0.1$ m (the same as that used in the present work). The test section is 1 m long and has a square cross-section with a side of 0.6 m. The flow turbulence level in the test section for the examined Reynolds number range is $0.2\ \% < Tu < 0.5\ \%$, with lower values of Tu having been measured at lower Reynolds numbers [19,21-22]. As reported in [9], the values of Tu were determined from data acquired at 5 kHz over a time window of 5 s. Measurements of the flow turbulence level were not repeated for the present study. Further details on the DNW-HDG wind tunnel, on its instrumentation and on the uncertainties in the test conditions are given in [17,19-24,32].

The examined two-dimensional model had the DU 91-W2-250 airfoil [8,13,21] as cross-section. This airfoil has a maximal thickness of 25 % c and is typically used in the mid-span region of modern wind-turbine rotor blades. The airfoil shape is displayed in Fig. 1a. The model chord length and the model span width were $c = 0.1$ m and $b = 0.6$ m, respectively. (The model thus spanned over the whole test section width, see above.)

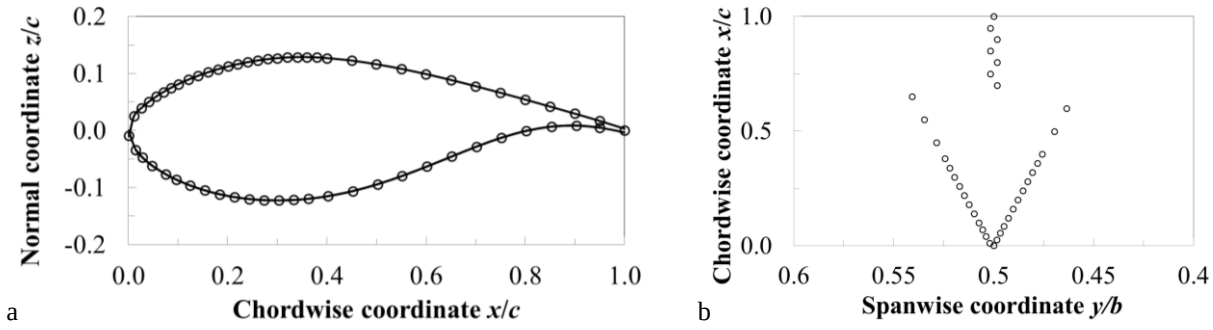

Fig. 1 a: DU 91-W2-250 airfoil contour (black line) and locations of the pressure taps (black circles); b: top view of the pressure tap locations on the model upper side. Axes not equally scaled.

The model was equipped with TSP to measure non-intrusively the surface temperature distribution on the model upper surface, and thus boundary-layer transition; moreover, TSP also allowed for the examination of separated flow regions at large angles-of-attack (see Secs. III and V). As compared to a typical TSP application in wind-tunnel testing [14,29,33], the composition of the coating layers was modified to integrate a layer of Carbon-Nanotubes (CNT) [17,20,34], in a manner analogous to that presented in [17,20]. The CNT layer served as electrical heating to impose a temperature difference (of approx. 1-1.5 K) between model surface and flow, thus enhancing the temperature difference between the laminar and turbulent flow domains close to the model surface and enabling global and reliable transition detection via TSP. (The temperature difference imposed between flow and model surface was proven to be sufficiently small to have no appreciable influence on boundary-layer transition.) To guarantee the adhesion of the TSP to the metallic surface, the model was firstly coated with a primer layer; a white screening layer for thermal insulation (which also functioned as a diffusive light-scattering background) was then applied on the primer layer; the layer of CNT was applied on this first screening layer; a second screening layer, with the same properties as the first one, was applied on the CNT layer; and finally the active layer, in which the luminophores were embedded, was applied on the screening layer. The final thickness of the five-layer TSP was approximately 270 μm. The TSP active layer was composed of a europium complex (luminophore) [35] incorporated in a commercial polyurethane clear-coat binder. The luminophore is excited in the wavelength range λ_{ex} = 350–450 nm and emits in the wavelength range λ_{em} = 600–630 nm. The TSP surface was polished to an average roughness value of R_a = 0.04 μm (mean roughness depth R_z = 0.2 μm): these roughness values are very low, and hence compatible with the thin boundary layer developing on the wind-tunnel model surface at the large Reynolds numbers considered in the present work.

An image of the experimental setup in the DNW-HDG test section, including the optical setup for TSP measurements, is shown in Fig. 2. Optical access to the wind-tunnel model is very limited at DNW-HDG because of the safety constraints due to the large pressure difference between the air inside and outside of the wind tunnel. The excitation light for the applied TSP was supplied by five light-emitting diodes (LEDs), with a specified excitation center wavelength of λ = 405 nm, which were installed behind glass windows mounted in the turntables. Band-pass filters for the wavelength range 375-415 nm were placed in front of the LEDs in order to block light at lower and higher wavelengths. The distribution of light emitted by the TSP was detected by means of a miniaturized charge-coupled device (CCD) camera, with a 12-bit dynamic range and a 1392 × 1024 pixel sensor. The camera was mounted inside a de-pressurized box, which was installed in the turntable at the starboard side wall of the test section. The camera was equipped with a 6.1 mm focal length pinhole lens, and a high-pass spectral filter (cut-off wavelength at λ = 590 nm) was mounted between the camera lens and the CCD chip. The optical filter allowed for capturing the light emitted by the TSP, while at the same time blocking light at shorter wavelengths. The angle between the camera axis and the model plane was approx. 27°. The oblique observation angle, together with the short focal length of the camera lens, caused a marked perspective distortion; the spatial resolution of the imaged model surface decreased with increasing distance of the model surface from the camera. On the other hand, with the used optical setup, neither the distribution of the excitation light supplied by the LEDs, nor the image of the model surface observed by the camera changed when the model angle-of-attack was varied, since the whole turntable including camera and LEDs rotated when this angle was changed. As described in [32], the TSP images were projected (mapped) onto a three-dimensional grid representing the model upper surface, according to the procedure discussed in detail in [36]. The mapped TSP images enabled accurate transition detection over most of the model span width (see Sec. III).

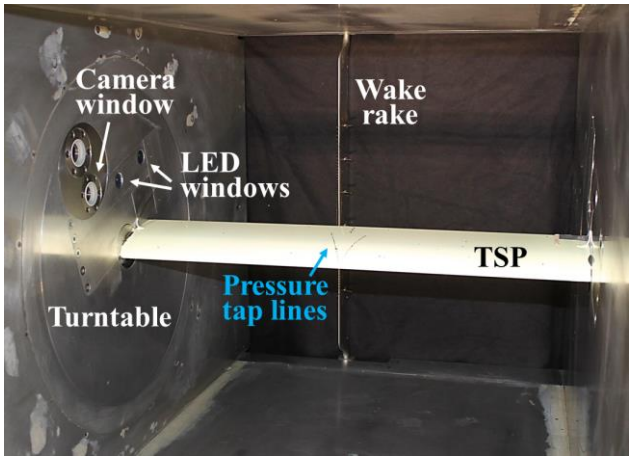

Fig. 2 Model mounted in the DNW-HDG test section, as seen from an upstream position.

As can be seen in Fig. 1 and Fig. 2, the model was also instrumented with pressure taps to measure the surface pressure distribution. The 61 pressure taps were installed in the model mid-span area and embedded in the TSP. The pressure taps coordinates along the airfoil contour are shown in Fig. 1a, whereas the distribution of the pressure taps in the streamwise and spanwise directions is shown in Fig. 1b. The pressure taps located in the region at $x/c \leq 65$ % were distributed in a staggered order, so that the measurement at any one tap was not affected by the disturbances caused by the upstream orifices, in a manner similar to that described, e.g., in [33]. The angle of these pressure tap lines about the vertical axis was approximately ±20° with respect to the freestream. The line of pressure taps located at $x/c > 65$ % was essentially parallel to the freestream: in this region, the boundary layer was expected to be turbulent at all test conditions examined in the present work, so that the measurements of these pressure taps were assumed to be not affected by the disturbances caused by the upstream orifices. The pressure sensors attached to the taps were scanned at 330 Hz for each channel using an 18-bit data acquisition system, which was equipped with temperature-compensated electronic pressure scanning modules with a nominal accuracy of ±103 Pa. The pressure measurements were averaged over an integration time of 20 s. The uncertainty in the measured model surface pressures was within ±0.7 %.

Each one of the DNW-HDG test-section upper and lower walls is equipped with 23 pressure taps to measure the wall pressure distribution in the freestream direction, which is used to evaluate and correct the influence of the wall interference on the measured model surface pressure distribution and aerodynamic coefficients [37]. However, because of the relatively small ratio between model chord length and test-section height (approx. 0.167), the corrections applied to the pressure distributions measured in the present work were less than ±2 %. The wind-tunnel wall pressure taps were acquired in the same way as the model pressures, except for the electronic pressure scanning modules, which had in this case a nominal accuracy of ±17 Pa.

The coefficients of airfoil lift (c_L) and pitching moment (c_m) were computed by integration of the measured surface pressure distribution. As shown in Fig. 2, a wake rake was also installed at $y/b = 66.7$ % downstream of the model, at a distance $\Delta(x/c) = 3.4$ downstream of the model trailing edge, to measure the airfoil drag. The airfoil drag coefficient (c_D) was computed with the measured pressures by using the momentum theorem. The uncertainty in the measured aerodynamic coefficients, with consideration of the whole measurement chain, was within ±0.7 %.

Further details on the experimental setup and on its accuracy are provided in [32].

III. Experimental Results

The experiments were conducted at Reynolds numbers Re = 3, 6, 9, and $12 \cdot 10^6$ (flow total pressure p_0 = 4.6 and 7.0 MPa), Mach numbers $0.03 \leq M < 0.1$, and angles-of-attack in the range $-14° \leq AoA \leq 20°$. The repeatability of the results was checked for each examined Reynolds number: the differences in the experimental data (aerodynamic coefficients and transition locations included) were shown to be within the corresponding measurement uncertainties. The evolution of the boundary layer with varying angle-of-attack and Reynolds number is presented with example data series in Secs. III.A and III.B, respectively.

A. Boundary-Layer Evolution with Varying Angle-of-Attack

The effect of a variation in the angle-of-attack on the evolution of the boundary layer over the examined area is shown here with an example series of TSP results obtained at $Re = 3 \cdot 10^6$ (M = 0.03) and angles-of-attack in the range $-12° \leq AoA \leq 20°$. The TSP results presented in Fig. 3 show the wind-tunnel model as it would be seen from the top wall of the DNW-HDG test section; they were achieved after the TSP images, acquired by the camera mounted at the turntable of the test-section side wall, had been mapped onto a three-dimensional grid representing the model upper surface (see Sec. II and [32]). The regions close to the test-section side walls (i.e., at $y/b \leq 19$ % and $y/b \geq 78$ %) were masked white, since these regions were not completely visible in the TSP images and/or their spatial resolution was too low. (As discussed in Sec. II, these limitations resulted from the restricted optical access in the DNW-HDG test section – see [32] for more details.) In Fig. 3, the flow is from the left; in the attached flow regions, bright and dark areas correspond to areas of smaller and larger heat flux, respectively, and therefore to areas of smaller and larger wall shear stress. This relationship between wall heat flux and wall shear stress applies also in separated regions (although the relationship may be more complex); therefore, at large angles-of-attack, separated regions of turbulent flow appear in the TSP results as brighter areas, as compared to the attached turbulent flow regions [38]. The representation of the TSP results used in Fig. 3 will be common to all the following TSP results presented in this work. Thus, bright and dark areas in Fig. 3a-e ($-12° \leq AoA \leq 10°$) correspond to laminar and turbulent regions, respectively. At larger angles-of-attack (AoA = 15° and 20°), the turbulent flow was found to separate, leading to the appearance in Fig. 3f-g of a bright region downstream of the darker region of attached turbulent flow. Moreover, a turbulent wedge is clearly visible in Fig. 3b-d, in the area between the staggered pressure tap lines. It was caused by disturbances originating from the pressure taps in the leading-edge region (see [33] and [36] for a similar finding).

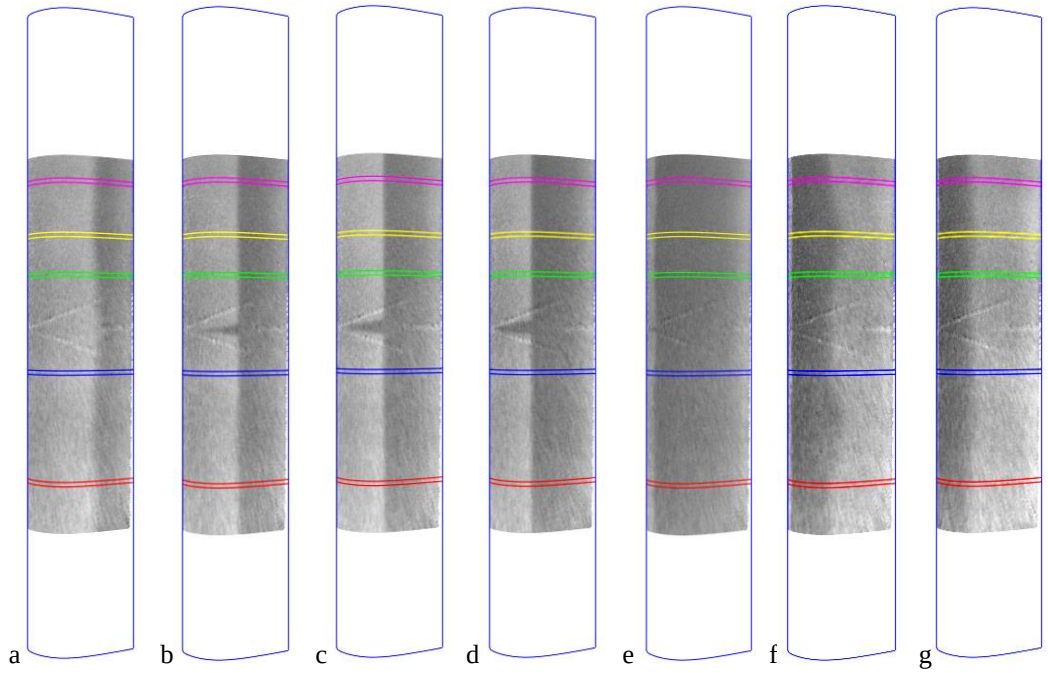

Fig. 3 TSP results obtained at Re = 3 · 10^6 (M = 0.03) for various angles-of-attack. The angles-of-attack, the detected transition locations and the estimated separation locations are reported in Table 1.

Table 1 Detected transition locations and estimated locations of turbulent separation for the cases of Fig. 3.

Fig.	AoA [°]	x_T/c	x_s/c (approx.)
3a	-12	64.3 ±1.3 %	-
3b	-6	52.9 ±0.3 %	-
3c	0	45.4 ±0.5 %	-
3d	5	40.4 ±0.3 %	-
3e	10	8.5 ±0.6 %	-
3f	15	~ 4 %	35-45 %
3g	20	~ 1 %	30 %

The transition locations x_T/c and the corresponding uncertainties reported in Table 1 were obtained as averages and standard deviations of the transition locations detected at five different evaluation sections, which were located at different spanwise positions and which bounds are indicated in Fig. 3 by two lines with the same color. (Averaging of transition locations to obtain a single value x_T/c was justified for the evaluated spanwise area, where the flow was essentially two-dimensional.) The spanwise locations of the evaluation sections were kept unchanged for all examined test conditions in order to obtain consistent results. At each spanwise position, the transition location was

detected as the location corresponding to the maximal gradient of the streamwise temperature distributions; this operation was performed automatically by means of a reliable algorithm described in [36,39]. The only constraint for the application of the algorithm was that the maximal temperature gradient was in the range 7 % ≤ x/c ≤ 93 %, since the number of available grid points upstream / downstream of the sought location would have been otherwise too small for reliable detection. In the cases at larger angles-of-attack, the approximate location of turbulent flow separation was estimated at the location of strongest TSP intensity change (i.e., from dark to bright in the figures). The estimated locations of turbulent separation are also reported in Table 1.

The pressure distributions on the model upper surface, measured simultaneously with the TSP data of Fig. 3, are presented in Fig. 4. In this and in the following graphical representations of the pressure distributions, the error bars (see Sec. II) are smaller than the symbol size and therefore not shown.

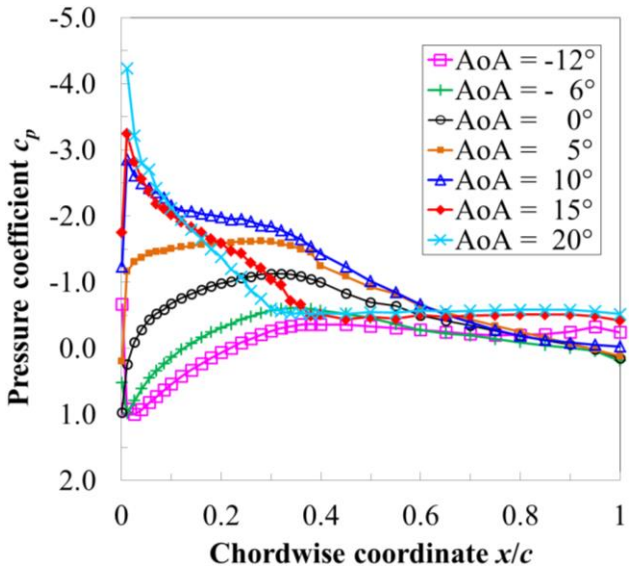

Fig. 4 Pressure distributions measured on the model upper surface for the cases of Fig. 3.

At AoA ≤ 5° (Fig. 3a-d), transition occurred in the region of adverse pressure gradient downstream of the pressure minimum, which magnitude increased at larger angles-of-attack but remained still moderate (see Fig. 4). The adverse pressure gradient at approx. $x/c \geq 30$ % became more pronounced with increasing AoA, leading to a shift of transition into a more upstream location: from x_T/c = 64.3 ±1.3 % at AoA = -12° (Fig. 3a) to x_T/c = 40.4 ±0.3 % at AoA = 5° (Fig. 3d). Note that, in spite of the large steps in AoA shown in Fig. 3a-d, the relative

variations in transition location were rather small, especially in the range of angles-of-attack at -6° ≤ AoA ≤ 5°. The variation of the transition location with increasing angle-of-attack was particularly small when compared with those observed on NLF airfoils [33]; this was clearly due to the different design objective of the examined DU 91-W2-250 airfoil, which was optimized for wind-turbine rotor blades [8,13]. Moreover, the transition front was an essentially straight line for AoA = -6°, 0°, and 5°, whereas it was slightly modulated in the spanwise direction at AoA = -12°: in this latter case, the adverse pressure gradient inducing boundary-layer transition was relatively weak, as compared to that at AoA ≥ -6° (see Fig. 4). This led to a transition front more similar to that observed, e.g., on flat-plate configurations [36] and on NLF airfoils in regions of analogously weak adverse pressure gradient [33]. It is also interesting to note that, at AoA = -12°, disturbances arising from the pressure taps in the leading-edge region did not lead to the formation of a turbulent wedge (see Fig. 3a), whereas in the TSP results at -6° ≤ AoA ≤ 5° a turbulent wedge was observed in the mid-span area of the model upper surface. (The apex of the turbulent wedge seems visible also at AoA = 10°.)

At AoA = 10° (Fig. 3e), the transition location was found at a significantly more upstream location (x_T/c = 8.5 ±0.6 %) than that presented in the previous cases. This was due to the major change in the streamwise pressure distribution, as compared to the cases at AoA ≤ 5° (see Fig. 4). In particular, the pressure minimum increased in magnitude, and was here located in the leading-edge region. The following, marked adverse pressure gradient in the streamwise direction led to earlier boundary-layer transition. Nevertheless, the turbulent boundary layer appeared to remain attached over the whole model upper surface even at such already large angle-of-attack. This was no longer the case at AoA = 15°. As can be seen in Fig. 3f (and in the estimated locations of turbulent separation reported in Table 1), the turbulent boundary layer was found to separate in the region 35 % ≤ x_s/c ≤ 45 %, resulting in a brighter region (i.e., a region of reduced wall heat flux [38]) downstream of the darker region of attached turbulent flow. The turbulent flow separation observed in the TSP results was confirmed by the pressure distribution shown in Fig. 4, where separation was detected at x_s/c ~ 40 %, i.e., at the location where the surface pressure distribution became uniform. It should be emphasized here that the separation front at AoA = 15° presented significant variations in the spanwise direction, as shown in Fig. 3f. This was likely due to the effect of three-dimensional structures in the separated flow regions, such as those found in [40] on another wind-turbine rotor-blade airfoil examined via oil-film visualizations in the same Reynolds number range, which were described as "mushroom-like" structures or "owl eyes". These flow structures are often referred to as "stall cells" and are typically most prominent at angle-of-attacks just beyond (static) stall conditions [41]. The use of the global, non-

intrusive TSP measurement technique enabled an improvement in the understanding of this complex flow scenario, which would have not been revealed by a single section of pressure taps. (Note that also pressure-sensitive paints can provide information on three-dimensional structures in separated flow regions, as shown, e.g., in [42].) In any case, it should be emphasized here that the reported TSP results were obtained from time-averaged measurements, i.e., from the average of 38 TSP images acquired at a frequency of approx. 3.1 Hz (CCD exposure time of 0.18 s) [32]. With the adopted experimental setup, it was not possible to capture the temporal development of the separated three-dimensional structures, as done for example in a laminar separation bubble [43] or in the separated turbulent flow [41] investigated in a water tunnel. At AoA = 15°, transition was observed at a location even more upstream than that found at AoA = 10°. The transition location was at approx. x_T/c = 4 %, but could not be accurately determined by means of the transition detection algorithm, as discussed above. This evolution of boundary-layer transition was clearly in agreement with the evolution of the surface pressure distribution at increasing angles-of-attack, and in particular with the upstream movement and magnitude increase of the pressure minimum, followed in the streamwise direction by a more pronounced adverse pressure gradient (see Fig. 4). Boundary-layer transition and turbulent separation were observed to move into a further upstream location as the angle-of-attack was increased to AoA = 20°. As can be seen in Fig. 3g and in Fig. 4, boundary-layer separation at the largest examined angle-of-attack was found at $x_s/c \sim 30$ %, whereas transition occurred just downstream of the leading edge. It should be also noted here that the separation front was more two-dimensional at AoA = 20° (Fig. 3g), as compared to the case at AoA = 15° (Fig. 3f).

In order to analyze in detail the onset of turbulent flow separation and the development of the separation front, the TSP results obtained at 10° ≤ AoA ≤ 13° are shown in Fig. 5. As already discussed above, the turbulent boundary layer on the model upper surface was still attached at AoA = 10° (Fig. 5a). At AoA = 11° (Fig. 5b), the turbulent boundary layer separated (stall conditions). As the angle-of-attack was increased from AoA = 11° to 12°, the spanwise distribution of the separation front in the mid-span model area changed – see Fig. 5b-c. In particular, at AoA = 12°, separation was seen at a more downstream location (by approx. $\Delta(x_s/c)$ = 10 %) in the region corresponding to the port pressure tap line, as compared to AoA = 11°. As the angle-of-attack was further increased to AoA = 13° (Fig. 5d), a major variation in the spanwise distribution of the separation front was observed: in the mid-span model region, separation occurred significantly more upstream (by approx. $\Delta(x_s/c)$ = 15 %), as compared to AoA = 12°; in contrast, separation was shifted significantly more downstream (interestingly, also by up to approx. $\Delta(x_s/c)$ = 15 %) in the region between the red and blue evaluation sections and in the region corresponding to the

yellow evaluation section. As the angle-of-attack was further increased to AoA > 13°, separation occurred at a more upstream location for larger AoA, but the spanwise distribution of the separation front initially remained very similar to that observed at AoA = 13°. This can be seen by comparing the TSP results at AoA = 13° (Fig. 5d) and AoA = 15° (Fig. 3f). However, as already discussed above with regard to Fig. 3g, the separation front became more two-dimensional at the largest angles-of-attack.

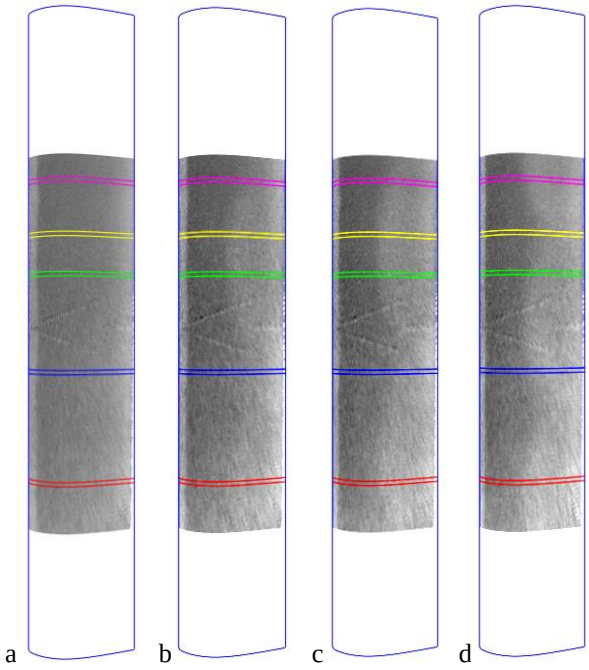

Fig. 5 TSP results obtained at Re = 3 · 10^6 for the following angles-of-attack: a: AoA = 10°, b: AoA = 11°, c: AoA = 12°, d: AoA = 13°.

The evolution of the boundary layer with increasing angle-of-attack described in this section for Re = 3 · 10^6 was basically similar for all examined Reynolds numbers, with some differences observed at large (AoA > 10°) and small (AoA < -8°) angles-of-attack. These different behaviors with increasing Reynolds number will be shown with three examples in the next section and further discussed in Sec. V.A.

B. Evolution of Boundary-Layer Transition with Varying Reynolds number

The influence of a change in the Reynolds number on the boundary-layer evolution is presented here for three representative angles-of-attack: AoA = -12°, 0°, and 12°. The Reynolds number was varied from Re = 3 to 12 · 10^6. (The corresponding change in the Mach number was from M = 0.03 to 0.09.)

AoA = -12°

As discussed in the previous section, boundary-layer transition was found to occur at AoA = -12° and Re = $3 \cdot 10^6$ in a region of weak adverse pressure gradient. With increasing Reynolds number, transition was observed to move into a more upstream location. This is shown by the TSP results in Fig. 6 and by the detected transition locations in Table 2: as the Reynolds number was increased from Re = 3 to $12 \cdot 10^6$, the transition location was shifted from x_T/c = 64.3 ±1.3 % (Fig. 6a) to x_T/c = 37.6 ±8.7 % (Fig. 6d). Note also that the spanwise variation of the transition front was more pronounced at the two larger Reynolds numbers, leading to a significant increase of the uncertainty in the reported transition locations. Another important effect of the increase in the Reynolds number was the reduction of the temperature difference between the surface regions corresponding to the laminar and turbulent boundary layers, resulting in a lower intensity difference in the TSP results (see Fig. 6). This was due to the influence of the larger shear stress (and hence heat flux) acting on the model surface at larger Reynolds numbers, which weakened the temperature difference between flow and model surface imposed by means of the CNT (see Sec. II and [32]). It can be also seen in Fig. 6 that a slightly darker region became more visible on the port half surface of the model (in the area between the red and blue evaluation sections) as the Reynolds number was increased. This slightly darker region was likely due to an inhomogeneity in the surface heating distribution. Although it cannot be excluded that the increased turbulence level in the DNW-HDG test section at larger Reynolds numbers [19,21-22] may have had a local influence, it should be noted that, for AoA ≥ -12°, the transition locations obtained at Re = 6 and $9 \cdot 10^6$ were verified in [44] to be essentially independent of the combination of p_0 and U_∞ chosen to set the Reynolds number. In any case, the evolution of this slightly darker region in the TSP results with varying Reynolds number will be the focus of future investigations.

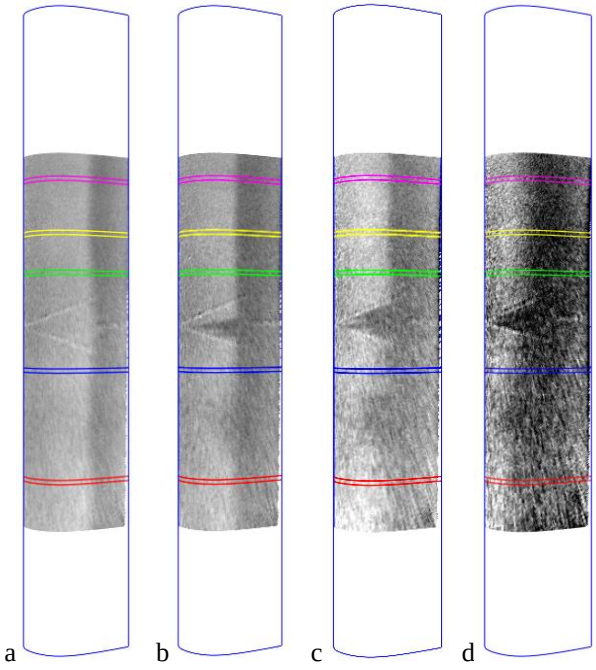

Fig. 6 TSP results obtained at AoA = -12° for various Reynolds numbers. The Reynolds numbers and the transition locations are reported in Table 2.

Table 2 Transition locations for the cases of Fig. 6.

Fig.	Re ($\cdot 10^6$)	x_T/c
6a	3	64.3 ±1.3 %
6b	6	54.8 ±1.0 %
6c	9	49.5 ±2.7 %
6d	12	37.6 ±8.7 %

The pressure distributions measured for the cases shown in Fig. 6 are presented in Fig. 7. The pressure distributions are in excellent agreement for $3 \cdot 10^6 \leq \mathrm{Re} \leq 9 \cdot 10^6$, with small differences (of the order of Δc_p = 0.03-0.05) observed only in the region 45 % $\leq x/c \leq$ 65 %. These differences were related to the different transition locations obtained at different Reynolds numbers (see [21] and [33] for similar findings). Larger surface pressures were measured at $\mathrm{Re} = 12 \cdot 10^6$, as compared to the values obtained at $3 \cdot 10^6 \leq \mathrm{Re} \leq 9 \cdot 10^6$. This difference was due to the significant changes in the pressure distribution on the model lower surface (not shown): more specifically, boundary-layer separation in the mid-span area was observed to occur at a more downstream location (by approx. $\Delta(x_s/c)$ = 10 %) than in the cases at $3 \cdot 10^6 \leq \mathrm{Re} \leq 9 \cdot 10^6$. This variation in boundary-layer evolution on the model lower surface influenced the whole airfoil circulation and therefore also the pressure distribution on the model upper

surface. Since an analogous variation in boundary-layer evolution was observed on the model upper surface for AoA = 12°, this behavior is discussed further below in this Section. In any case, the (weak) adverse streamwise pressure gradient in the transition region was nearly the same for all examined Reynolds numbers. For this boundary-layer stability situation at the DNW-HDG flow turbulence level (see Sec. II), transition is expected to occur as the result of the amplification of initially two-dimensional Tollmien-Schlichting (TS) instability waves [12,31,36,45], which was enhanced by an increase in the Reynolds number and thus led to earlier transition. This aspect is further discussed in Sec. IV.B.

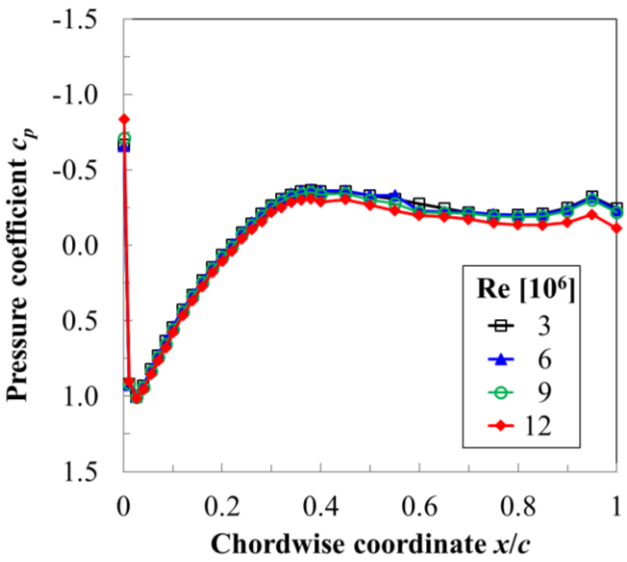

Fig. 7 Pressure distributions measured on the model upper surface for the cases of Fig. 6.

AoA = 0°

In the second examined series of results, at an angle-of-attack of AoA = 0°, the upstream shift in transition location observed at larger Reynolds numbers was relatively small. As can be seen in the TSP results shown in Fig. 8 and in the values of x_T/c reported in Table 3, the change in transition location was approx. $\Delta(x_T/c) = 6.3$ % for an increase in Reynolds number from Re = 3 to $12 \cdot 10^6$. Also the corresponding pressure distributions, measured on the model upper surface for the different Reynolds numbers and presented in Fig. 9, are in excellent agreement, except for the pressure measured at $x/c = 40$ %. The difference at this location was likely due to the influence of the wider turbulent wedge arising from the pressure taps in the mid-span area, which can be seen by a comparison of Fig. 8d with Fig. 8a-c. In contrast to the previous results obtained at AoA = -12°, in the present cases at AoA = 0° the

transition front did not show appreciable variations as the Reynolds number was increased, i.e., it remained an essentially straight line. Moreover, as compared to the cases at AoA = -12°, the aforementioned reduction of the efficiency of the imposed surface heat flux at larger Reynolds numbers had a weaker influence on the quality of the TSP results obtained in this transition scenario, in which transition was induced by a stronger adverse pressure gradient downstream of the pressure minimum. Note, however, that the slightly darker region on the port half surface, discussed above with regard to the cases at AoA = -12°, was confirmed to become more visible in the TSP results as the Reynolds number was increased.

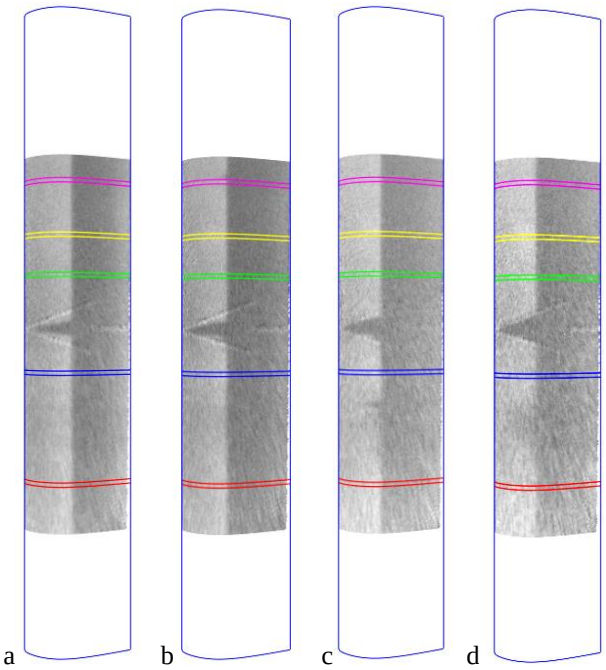

Fig. 8 TSP results obtained at AoA = 0° for various Reynolds numbers. The Reynolds numbers and the transition locations are reported in Table 3.

Table 3 Transition locations for the cases of Fig. 8.

Fig.	Re ($\cdot 10^6$)	x_T/c
8a	3	45.4 ±0.5 %
8b	6	42.6 ±0.7 %
8c	9	40.8 ±0.4 %
8d	12	39.2 ±0.6 %

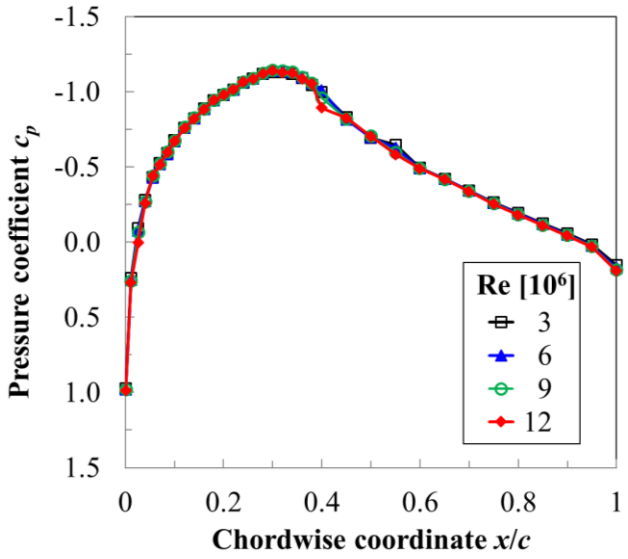

Fig. 9 Pressure distributions measured on the model upper surface for the cases of Fig. 8.

AoA = 12°

The third series of results considered in this section was obtained at AoA = 12°. As can be seen in the TSP results in Fig. 10, at this large angle-of-attack, transition occurred at a location very close to the leading edge. A short extent of laminar flow was found at the lowest Reynolds number Re = $3 \cdot 10^6$, with transition observed at approx. x_T/c = 6 %. The streamwise extent of the laminar flow region was further reduced as the Reynolds number was increased: at the two larger Reynolds numbers, the boundary layer underwent transition at a location just downstream of the leading edge. Nevertheless, the boundary-layer development over the model upper surface was still markedly influenced by a variation in the Reynolds number: in this case, the major influence of an increase in Re was not on laminar-turbulent transition, but rather on turbulent separation. At the two lower Reynolds numbers, the turbulent boundary layer was found to separate approximately in the mid-chord region; this resulted into to a brighter area over the downstream half surface, visible in the TSP data shown in Fig. 10a-b. (The estimated locations of turbulent separation are reported in Table 4.) In contrast, the flow was observed to remain attached over the whole model upper surface at the two larger Reynolds numbers (see Fig. 10c-d). This different behavior was confirmed by a look at the surface pressure distributions on the model upper surface, which are presented in Fig. 11. Boundary-layer separation was seen in the pressure tap region at approx. 45 % $\leq x_s/c \leq$ 55 % for Re = 3 and $6 \cdot 10^6$, whereas the pressure distributions at Re = 9 and $12 \cdot 10^6$ did not show regions of separated turbulent flow. These two latter pressure distributions were in excellent agreement (except for one pressure tap at x/c = 8.5 %), while differences

were observed with and between the pressure distributions obtained at Re = 3 and $6 \cdot 10^6$. This was clearly due to the separated flow conditions found at these two lower Reynolds numbers: as it will be shown with the lift coefficients presented in Sec. V.A, these two cases corresponded already to post-stall conditions. In contrast, the stall conditions for Re = 9 and $12 \cdot 10^6$ were reached at an angle-of-attack larger than that considered here. (The maximum lift coefficient was indeed measured at AoA = 12° and 13° for Re = 9 and $12 \cdot 10^6$, respectively.) In Fig. 10a-b it should be also noted that the separated flow region presented a three-dimensional character, which induced significant spanwise variations in the boundary-layer development even upstream of the separation location. These led to a "zig-zag" pressure distribution, visible in Fig. 11 for Re = 3 and $6 \cdot 10^6$. This "zig-zag" appearance was related to the different pressure distributions measured in the region 20 % $\leq x/c \leq$ 65 % by the two pressure tap lines (see Sec. II) for this three-dimensional boundary layer. Since only every second datapoint in Fig. 11 pertains to the same pressure tap line, the difference between the pressure distributions developing along the two tap lines led to the appearance of small "jumps" between successive pressure tap locations. At $x/c >$ 65 %, the only pressure tap line was nearly aligned with the freestream, so that spanwise flow variations could not be captured by the pressure taps.

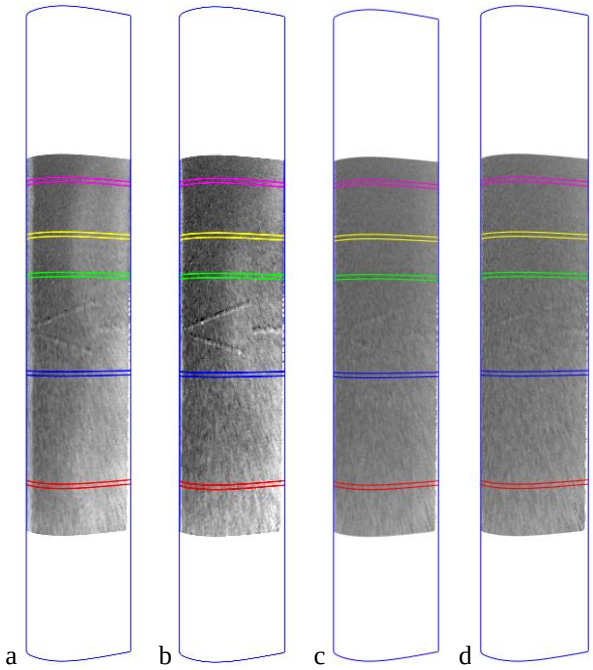

Fig. 10 TSP results obtained at AoA = 12° for various Reynolds numbers. The Reynolds numbers and the estimated locations of turbulent separation are reported in Table 4.

Table 4 Estimated locations of turbulent separation for the cases of Fig. 10.

Fig.	Re (· 10^6)	x_s/c (approx.)
10a	3	45-55 %
10b	6	45-55 %
10c	9	-
10d	12	-

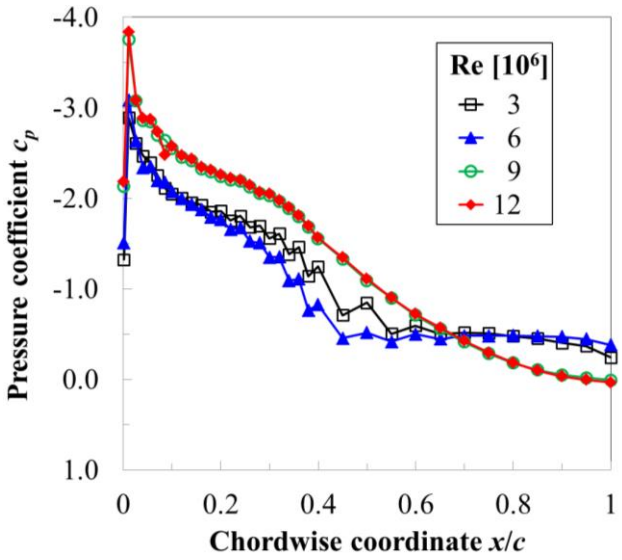

Fig. 11 Pressure distributions measured on the model upper surface for the cases of Fig. 10.

IV. Boundary-Layer Stability Analysis

The measured surface pressure distributions were used to carry out boundary-layer calculations by means of the boundary-layer solver COCO [46], which is a program to compute the wall-normal velocity profiles of steady, laminar boundary layers along swept, conical wings. In the case of a two-dimensional airfoil model, such as that examined in the present work, the boundary-layer equations appear as the limiting case of the equations for an infinite swept wing, which are a specific case of the equations for a conical wing. The distributions of boundary-layer displacement thickness δ_1 (solid line) and friction coefficient c_f (dashed line) for the case at Re = $3 \cdot 10^6$ and AoA = 0° (see Sec. III) are shown in Fig. 12a. Note that data are available only up to x/c = 40 %, since laminar separation due to the adverse pressure gradient was predicted by COCO at this chordwise location (shown by a vertical gray bar in Fig. 12a).

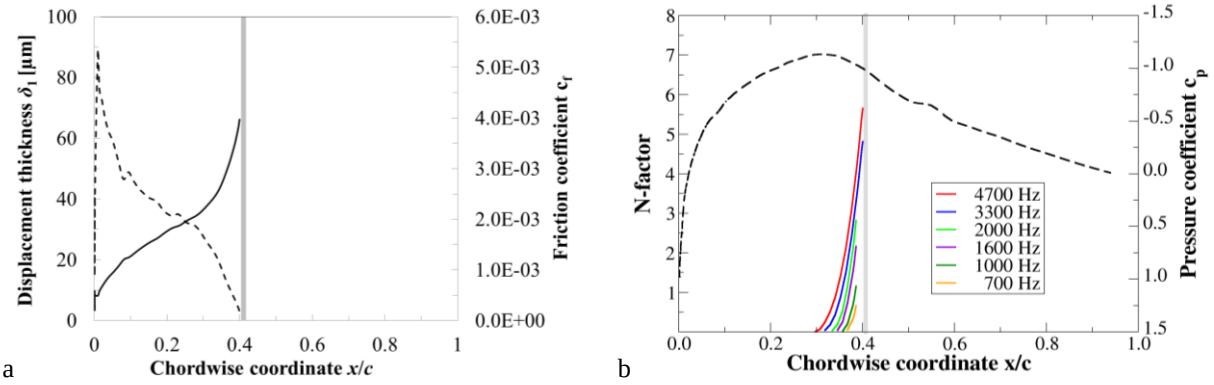

Fig. 12 Results of boundary-layer computations (a) and linear stability analysis (b) for the case at $Re = 3 \cdot 10^6$ (M = 0.03) and AoA = 0°. Boundary-layer displacement thickness δ_1 and friction coefficient c_f in Fig. 12a are shown by solid and dashed lines, respectively.

The stability of the computed boundary layer was then examined using the stability-analysis tool LILO [47]. The amplification factors (N-factors) [31] of two-dimensional Tollmien–Schlichting waves [12,31] were calculated for waves with different frequencies, according to incompressible, linear stability theory and assuming the flow as locally parallel. Since the temperature difference between model surface and flow was small [32], in the stability computations the surface was reasonably assumed as adiabatic. The distributions of N-factors obtained for the case at $Re = 3 \cdot 10^6$ and AoA = 0° are shown in Fig. 12b. Distributions of N-factors calculated for waves with different frequencies are shown by lines with different colors, whereas the dashed black line shows the examined pressure distribution. The predicted separation location is indicated by a vertical gray bar. Amplification of TS waves was found to start at $x/c \geq 30$ %, i.e., downstream of the pressure minimum; the amplification was observed to be very pronounced, showing a steep gradient of N-factors up to the predicted separation location.

The results of the boundary-layer stability analysis were correlated with the experimentally determined transition locations to obtain the maximal N-factor at the transition location [31,45,48], i.e., the transition N-factor N_T. The transition N-factors obtained for the various cases examined in this work will be presented in Sec. V.C. It should be however noted here that, in some cases, the measured transition location was further downstream of the predicted location of laminar separation. This was observed also for the case shown in Fig. 12b: transition was measured at $x_T/c = 45.4 \pm 0.5$ % (see Fig. 3c and Fig. 8a), whereas the predicted separation location was at $x/c = 40$ %. In these cases, the value of N_T was taken as the value of the maximal N-factor just upstream of the predicted separation

location (N_T = 5.7 in the case shown in Fig. 12b). Moreover, in most of the examined cases, the streamwise gradients of the N-factor distributions were probably too large for an adequate calibration of the transition N-factor [36,45]. Although in the literature there is no clear indication of a range of N-factor gradients adequate for the N_T-calibration, a change of $\Delta N \sim 1.5$ every $\Delta(x/c) \sim 1$ % was reported in [45] as "not suitable", while variations of the order of $\Delta N \sim 0.3$-0.5 every $\Delta(x/c) \sim 1$ % were considered as appropriate, e.g., in [49,50]. In the case shown in Fig. 12b, the N-factor changes by $\Delta N \sim 0.8$ every $\Delta(x/c) \sim 1$ %, i.e., the gradient $\Delta N/\Delta(x/c)$ was larger than the appropriate range from [49,50]. This was generally the case when transition was induced by a marked adverse pressure gradient, and especially when the laminar boundary layer was predicted to separate, such as in the case presented in Fig. 12b. For the cases in which this situation occurred, the reported values of N_T can be estimated to deviate by $\Delta N_T \sim 2$ (in some cases up to $\Delta N_T \sim 4$) from the value that they would have reached at the transition location, according to the gradient $\Delta N/\Delta(x/c)$ and the chordwise distance between the locations of predicted separation and measured transition. On the other hand, the gradient $\Delta N/\Delta(x/c)$ was within the aforementioned appropriate range in the cases with transition occurring in a region of less pronounced adverse pressure gradient (see, e.g., the case at AoA = -12° and $Re = 3 \cdot 10^6$ in the following Fig. 13). In these cases, the uncertainty in the determined values of the transition N-factor was estimated to be $\Delta N_T \sim \pm 0.5$, according to the gradient $\Delta N/\Delta(x/c)$ and the measurement uncertainty in the transition location.

Independently from the above considerations regarding the determined values of N_T, the results of linear stability computations were useful for the analysis of the sensitivity of the transition location to changes in angle-of-attack and Reynolds number, as discussed in the following sections.

A. Results of Boundary-Layer Stability Computations with Varying Angle-of-Attack

The results of boundary-layer stability analysis for the cases examined in Sec. III.A (Fig. 3) are presented in Fig. 13, where only the N-factor envelope curves computed for the various angles-of-attack are shown. These are the curves connecting the maxima of the N-factor for all amplified TS waves at each streamwise location. The stability computations were not performed for the larger angles-of-attack AoA = 15° and 20°, since boundary-layer transition occurred just downstream of the leading edge (see Fig. 3f-g): a stability analysis for a laminar boundary layer would have not been meaningful in these cases. The transition locations measured at $-12° \leq AoA \leq 10°$ are also indicated in Fig. 13, while the determined transition N-factors are reported in Table 5.

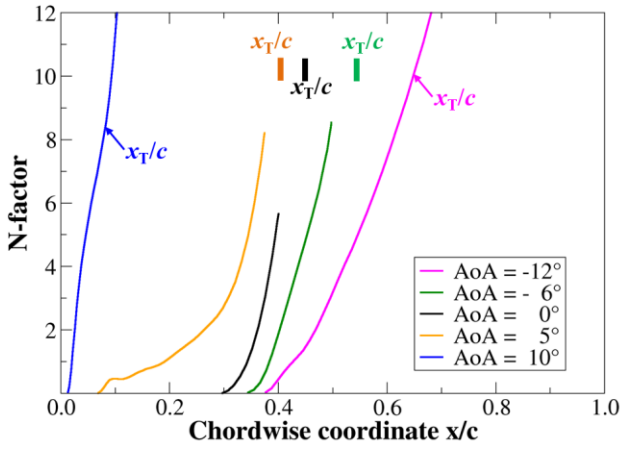

Fig. 13 N-factor envelope curves computed for the cases of Fig. 3 and Fig. 4. The transition N-factors are reported in Table 5.

Table 5 Transition N-factors for the cases of Fig. 13.

AoA [°]	x_T/c	N_T
-12	64.3 %	10.2
-6	52.9 %	8.5
0	45.4 %	5.7
5	40.4 %	8.1
10	8.5 %	8.5

Laminar separation was predicted upstream of the measured transition location for three of the examined cases (i.e., at $-6° \leq \text{AoA} \leq 5°$). In spite of this, the N-factor envelope curves were helpful to understand the transition development with increasing angle-of-attack, which was described in Sec. III.A. At larger AoA, the location of indifferent stability of Tollmien-Schlichting waves was shifted more upstream, i.e., the boundary-layer disturbance amplification started earlier. Moreover, the streamwise gradient of the N-factor envelope curves generally increased with increasing angle-of-attack. In the e^N method for transition prediction [31,45,48], transition is assumed to occur when a certain transition N-factor is reached. The average transition N-factor for the five cases of Fig. 13 was $N_T = 8.2$, with a standard deviation of $\Delta N_T = \pm 1.4$. By taking $N_T = 8.2$ as "the" transition N-factor for all five cases, transition would have been predicted to occur at a more upstream location with increasing AoA because of the two aforementioned effects: upstream shift of the indifferent-stability location and increase of the streamwise gradient of the N-factor distributions. This expected trend was in agreement with the experimental observations.

B. Results of Boundary-Layer Stability Computations with Varying Reynolds number

In this section, results of boundary-layer stability analysis for varying Reynolds number are presented for the first two series of results examined in Sec. III.B. Stability computations were not performed for the cases at AoA = 12°, since the boundary layer underwent transition in the leading-edge region (see Fig. 10).

AoA = -12°

The N-factor envelope curves computed for the cases at AoA = -12° are presented in Fig. 14, where the measured transition locations are also shown. The corresponding transition N-factors are reported in Table 6. As can be seen in Fig. 14, a larger Reynolds number led to earlier amplification of Tollmien-Schlichting waves [12,31] and to a general increase of the streamwise gradient of the N-factor envelope curves. According to the e^N method introduced in Sec. IV.A, transition is assumed to occur when the amplification factors reach a certain threshold N_T, which can be taken here as the average transition N-factor for the range $3 \cdot 10^6 \leq \mathrm{Re} \leq 9 \cdot 10^6$: $N_T = 8.2$. (The corresponding standard deviation is $\Delta N_T = \pm 1.4$.) The value of $N_T = 8.2$ would have been reached at a more upstream location as the Reynolds number was increased, leading to an upstream shift of the transition location. This trend, expected from linear stability theory combined with the e^N method, was in agreement with the experimental data. Note that the case at $\mathrm{Re} = 12 \cdot 10^6$ was not included in these considerations: although also in this case the upstream movement of the transition location was in line with the expectations presented above, transition occurred in the experiment at a location close to the indifferent-stability point (the distance between these two locations was $\Delta(x/c) \sim 3$ %). Only moderate amplification of TS waves would have been possible up to the measured transition location, leading to a very small transition N-factor of $N_T = 1.5$. As discussed above, however, such steep N-factor envelope curves are probably not adequate for the calibration of the transition N-factor, and this may have been the reason for the observed differences. In fact, the value of $N_T = 1.5$ was determined at the average transition location $x_T/c = 37.6$ %. In this case, the uncertainty in x_T/c was large ($\Delta(x_T/c) = \pm 8.7$ %, see Fig. 6), and the variation of the N-factors within the region of measurement uncertainty is also large (because of the steep N-factor envelope curve). A transition N-factor of $N_T = 6.2$, closer to the average N_T reported above for $3 \cdot 10^6 \leq \mathrm{Re} \leq 9 \cdot 10^6$, would have been indeed obtained at end of the measurement uncertainty region. The observed trend would thus have been similar to that seen at the lower Reynolds numbers. Nevertheless, the values of N_T obtained over the whole measurement uncertainty range of the transition location were still smaller than those found in the measurement uncertainty range at $3 \cdot 10^6 \leq \mathrm{Re} \leq 9 \cdot 10^6$. This was likely due to the larger turbulence level within the DNW-HDG test section at

Re = 12 · 10^6 (see Sec. II and [19,21-22]). The larger level of external disturbances probably led to a larger initial amplitude of the boundary-layer disturbances and thus to smaller N-factor values in the transitional region [31,45,48]. The validity of this conjecture will be verified with dedicated investigations in the future.

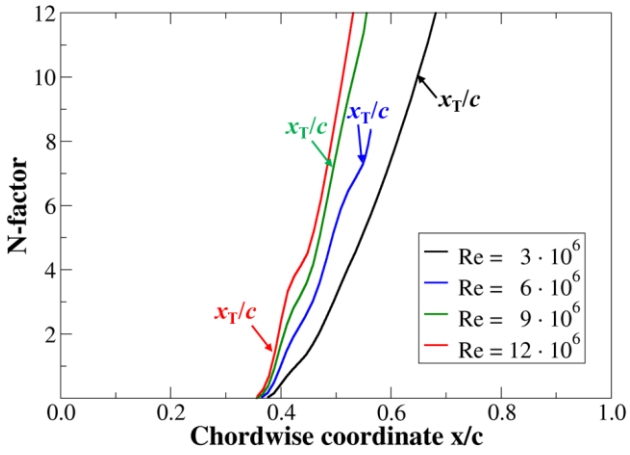

Fig. 14 N-factor envelope curves computed for the cases of Fig. 6 and Fig. 7. The transition N-factors are reported in Table 6.

Table 6 Transition N-factors for the cases of Fig. 14.

Re (· 10^6)	x_T/c	N_T
3	64.3 %	10.2
6	54.8 %	7.3
9	49.5 %	7.3
12	37.6 %	1.5

AoA = 0°

The results of boundary-layer stability analysis for the cases at AoA = 0° are presented in Fig. 15 for the Reynolds numbers Re = 3, 6, and 9 · 10^6, in a manner analogous to that of Fig. 14. As already discussed in Sec. IV.A, at the lowest Reynolds number (Re = 3 · 10^6) transition was measured downstream of the predicted location of boundary-layer separation. A similar behavior was also observed at Re = 6 and 9 · 10^6. The values of N_T reported in Table 7 are the maximal N-factors just upstream of the predicted separation location, and are therefore expected to be smaller than those that would have been obtained at the transition locations, which were more downstream (see discussion with regard to Fig. 12b). In spite of this, the results of the boundary-layer stability

computations show that the amplification of Tollmien-Schlichting waves started at a more upstream location as the Reynolds number was increased. (The gradients of the N-factor envelope curves appear to be similar after some distance from the indifferent-stability location.) By considering the e^N method for transition prediction and assuming a transition N-factor of $N_T = 5.7$ (corresponding to the maximal N-factor just upstream of the predicted separation location for the case at $Re = 3 \cdot 10^6$), transition was expected to move towards a more upstream location at larger Reynolds numbers. At the same time, the shift of the transition location was also expected to be small, since the N-factor envelope curves were steep in the examined region. These trends were in agreement with the measured shift of the transition location: transition was found at a more upstream location as the Reynolds number was increased, but this shift was only $\Delta(x_T/c) = 4.6$ % as the Reynolds number was increased from $Re = 3$ to $9 \cdot 10^6$ (see Fig. 8). The resolution of the measured surface pressure distribution in the region of disturbance amplification for the case at $Re = 12 \cdot 10^6$ appeared to be not suitable for the linear stability computations; the N-factor envelope curves are therefore not available for this case. The expected trend would be, however, similar to that discussed above for the lower Reynolds numbers, and thus in line with the observed small upstream shift of the transition location: in fact, transition was measured at a location approx. $\Delta(x_T/c) = 2$ % more upstream than that found at $Re = 9 \cdot 10^6$.

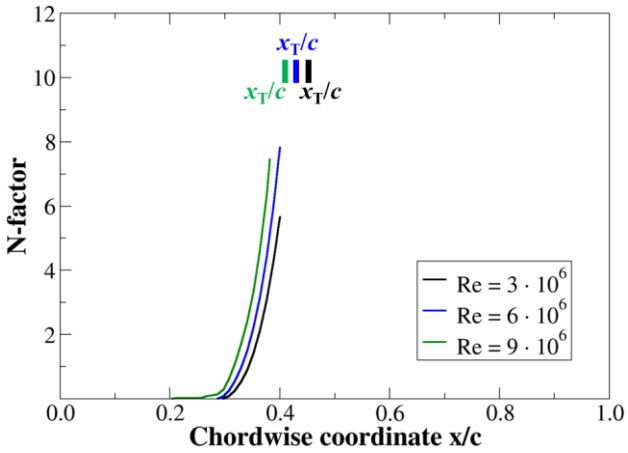

Fig. 15 N-factor envelope curves computed for the cases of Fig. 8 and Fig. 9. The transition N-factors are reported in Table 7.

Table 7 Transition locations for the cases of Fig. 15.

Re ($\cdot 10^6$)	x_T/c	N_T
3	45.4 %	5.7
6	42.6 %	7.8
9	40.8 %	7.5

V. Discussion

The discussion of the results is subdivided into three sections. In the first section (Sec. V.A), the evolution of the aerodynamic coefficients is analyzed for varying angles-of-attack and different Reynolds numbers; this is accomplished also with the support of the global information on laminar-turbulent transition and turbulent separation from the TSP results. The evolution of boundary-layer transition on the model upper surface is discussed in Sec. V.B. Finally, the transition N-factors determined on the model upper surface are presented and discussed in Sec. V.C.

A. Evolution of the Aerodynamic Coefficients

The coefficients of lift, pitching moment, and drag are presented as a function of the angle-of-attack in Fig. 16a, Fig. 16b, and Fig. 16c, respectively. Different colors show data obtained at different Reynolds numbers.

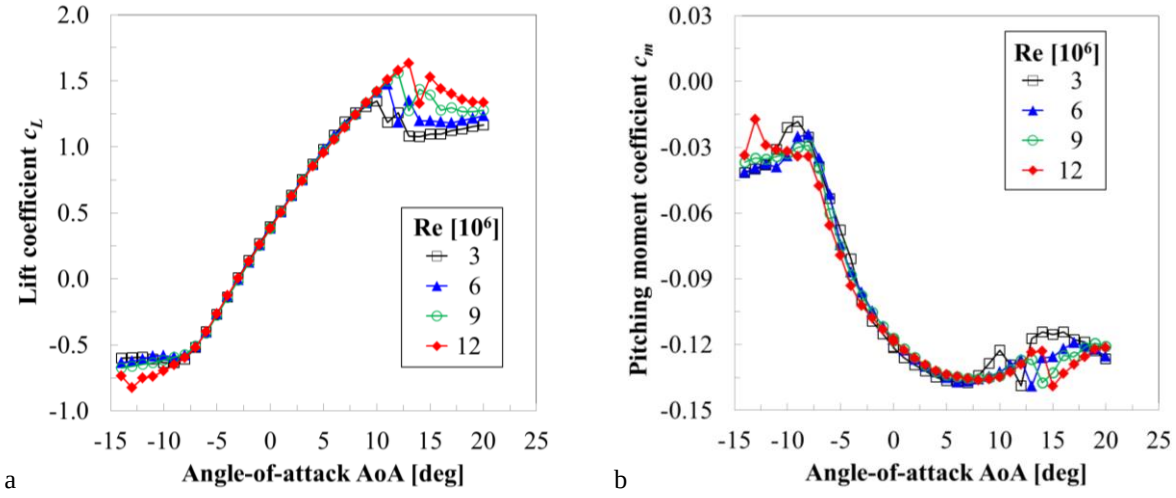

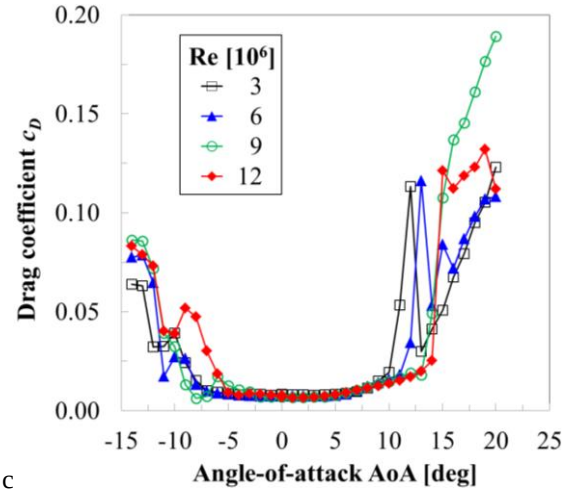

c

Fig. 16 Aerodynamic coefficients measured at various angles-of-attack and Reynolds numbers. a: lift coefficient; b: pitching moment coefficient; c: drag coefficient.

The discussion of the evolution of the aerodynamic coefficients at different Reynolds numbers is presented in the following for three ranges of angles-of-attack. This conceptual subdivision, however, should be regarded as a qualitative support to the discussion. In particular, the limits of the different AoA-ranges depend on the Reynolds number and on the considered aerodynamic coefficient.

Moderate Angles-of-Attack

As can be seen in Fig. 16a, the lift coefficient showed a nearly-linear dependency on the angle-of-attack in the range $-6° \leq \text{AoA} \leq 6°$. At larger and smaller angles-of-attack, the function $c_L(\text{AoA})$ deviated from this quasi-linear behavior. The lift coefficients measured at the different Reynolds numbers were in agreement in the quasi-linear range of the $c_L(\text{AoA})$ curve: the differences in the lift coefficients at $-6° \leq \text{AoA} \leq 6°$ were generally less than 5 % of the measured values, and in most cases below 2 %. Accordingly, the variation of the (average) slope of the lift coefficient curve in the range $-6° \leq \text{AoA} \leq 6°$ was less than 2.5 % for the examined Reynolds numbers. The relative differences in the values of c_L remained below 5 % up to AoA = 10°, i.e., up to the angle-of-attack corresponding to $c_{L,\max}$ at $\text{Re} = 3 \cdot 10^6$.

The evolution of c_m as a function of the angle-of-attack in the range $-8° \leq \text{AoA} \leq 10°$ (Fig. 16b) was similar for all examined Reynolds numbers: c_m decreased continuously with increasing angle-of-attack up to AoA = 7°, and then increased at larger AoA up to the angle-of-attack corresponding to $c_{L,\max}$ (at $\text{Re} = 3 \cdot 10^6$) or to stall conditions (at

$6 \cdot 10^6 \leq Re \leq 12 \cdot 10^6$ – see below). Small differences of less than 5 % (and in most cases of less than 2 %) were observed for the pitching moment coefficients in the range of angles-of-attack $-3° \leq AoA \leq 9°$.

As shown in Fig. 16c, the drag coefficient remained small for all examined Reynolds numbers in the range of angles-of-attack $-4° \leq AoA \leq 4°$, and increased at larger and smaller angles-of-attack. In the range of angles-of-attack $-3° \leq AoA \leq 9°$ considered above with regard to the pitching moment coefficients, the differences in the drag coefficients measured at different Reynolds numbers were generally larger than those found for c_L and c_m: they were of the order of 5-10 % of the measured values. In any case, the evolution of the drag coefficient at $-4° \leq AoA \leq 10°$ was similar for all examined Reynolds numbers.

It should be emphasized that, in the aforementioned ranges of angle-of-attack, the aerodynamic coefficients obtained after integration of the pressure distributions measured on the surface and in the wake of the model were representative for the evolution of the airfoil performance, since the flow had remained essentially two-dimensional.

Angles-of-Attack Corresponding to $c_{L,max}$, Stall, and Post-Stall Conditions

Larger differences in the aerodynamic coefficients measured at the four different Reynolds numbers were observed at $AoA \geq 10°$. The angle-of-attack corresponding to $c_{L,max}$ increased consistently by $\Delta AoA = 1°$ for each increase $\Delta Re = 3 \cdot 10^6$ in the Reynolds number. Moreover, the maximal value of the lift coefficient also increased by approx. $\Delta c_{L,max} = 0.1$ for each increase $\Delta Re = 3 \cdot 10^6$ in the Reynolds number: from $c_{L,max} = 1.35$ (at $AoA = 10°$) for $Re = 3 \cdot 10^6$ to $c_{L,max} = 1.63$ (at $AoA = 13°$) for $Re = 12 \cdot 10^6$. These findings were in agreement with those reported in earlier work [21].

At stall and post-stall conditions, the interpretation of the measured aerodynamic coefficients would have been difficult without the support of the TSP results. In fact, the evolution of c_L, c_D, and c_m was markedly influenced by turbulent flow separation, which introduced a significant three-dimensionality into the boundary-layer development over the model upper surface, leading to spanwise variations of the separation front. Moreover, the streamwise extent of the separated flow region and the spanwise distribution of the separation front varied with increasing angle-of-attack and with increasing Reynolds number. The evolution of c_L and c_m was therefore representative only for the local flow development in the mid-span model region, i.e., in the region of the pressure tap lines; analogously, the evolution of c_D was representative only for the local flow development around $y/b = 66.7$ %, i.e., the spanwise location corresponding to the installation position of the wake rake. The TSP results thus provided not only global information on the boundary-layer development over the model upper surface (especially in terms of global

identification of laminar-turbulent transition and turbulent separation), but also an explanation for the observed evolution of the lift, drag, and pitching moment coefficients at stall and post-stall conditions. This is exemplarily discussed for the case at $Re = 3 \cdot 10^6$. As shown in Sec. III.A, the turbulent boundary layer on the model upper surface was still attached at AoA = 10° (Fig. 5a): this was the condition corresponding to $c_{L,max}$. The onset of turbulent flow separation at AoA = 11° (Fig. 5b) led to the drop in lift and pitching moment coefficients in Fig. 16a-b as well as to the jump in the drag coefficient in Fig. 16c. The re-increase of c_L, observed as the angle-of-attack was varied from AoA = 11° to 12°, was due to the local change of the spanwise distribution of the separation front in the mid-span model area – see Fig. 5b-c. The following variation in the values of the aerodynamic coefficients, as the angle-of-attack was further increased to AoA = 13°, was also due to the change in the spanwise distribution of the separation front. In the mid-span model region, the upstream shift of the separation location (Fig. 5c-d) led to the observed decrease in c_L and increase in c_m. In contrast, c_D decreased as the angle-of-attack was increased from AoA = 12° to 13°; this was due to the downstream shift of the separation location in the area corresponding to the installation position of the wake rake (region around the yellow evaluation section in Fig. 5c-d). As the angle-of-attack was then increased to AoA > 13°, separation occurred at a more upstream location for larger AoA, but the spanwise distribution of the separation front remained basically the same as that seen at AoA = 13°. For this reason, the evolution of the aerodynamic coefficients at AoA > 13° did not show any further abrupt changes.

The evolution of the separated flow region on the model upper side had the predominant influence on the evolution of the measured aerodynamic coefficients at stall and post-stall conditions also for $Re = 6, 9$ and $12 \cdot 10^6$. A detailed discussion of the values of c_L, c_m, and c_D, obtained at these conditions after integration of the local measurements via pressure sensors, is not presented here, since it would lead to an excessively long manuscript. In any case, it should be emphasized that the TSP-based, global information on the evolution of the turbulent separation front provided an explanation for the evolution of the measured aerodynamic coefficients at $AoA \geq 10°$ for all examined Reynolds numbers.

Markedly Negative Angles-of-Attack

As can be seen in Fig. 16a-b, the evolution of the lift and pitching moment coefficients at $AoA \leq -9°$ was similar for the Reynolds number range $3 \cdot 10^6 \leq Re \leq 9 \cdot 10^6$, and different from that obtained at $Re = 12 \cdot 10^6$. It can be expected here that, at $AoA \leq -9°$, the evolution of the separated flow region in the mid-span area of the model lower surface was similar for the three lower Reynolds numbers and different from that at the largest Reynolds number. In

the mid-span area, this expectation was confirmed by the analysis of the lower surface pressure distribution, as discussed for AoA = -12° in Sec. III.B. At the negative angles-of-attack, the drag coefficients increased significantly at approx. AoA < -7° for the Reynolds numbers $3 \cdot 10^6 \leq \mathrm{Re} \leq 9 \cdot 10^6$, whereas the increase in c_D had been already observed at AoA < -5° at $\mathrm{Re} = 12 \cdot 10^6$ (see Fig. 16c). This difference was likely due to the different evolution of the transition location on the model upper surface observed for the largest Reynolds number at AoA < -5°, as compared to that found at the lower Reynolds numbers (see Sec. V.B). While transition occurred at a more downstream location with decreasing angle-of-attack at $3 \cdot 10^6 \leq \mathrm{Re} \leq 9 \cdot 10^6$, the transition location at $\mathrm{Re} = 12 \cdot 10^6$ remained nearly constant up to AoA = -8°, and moved even further upstream at smaller angles-of-attack. In any case, the evolution of the drag coefficient at AoA ≤ -9° was probably dominated by the evolution of the separated flow region on the model lower surface. This model surface will be the main subject of future experiments in DNW-HDG.

B. Evolution of the Boundary-Layer Transition

The transition locations measured by means of the TSP technique are plotted as a function of AoA in Fig. 17, where different colors show data obtained at different Reynolds numbers. It is recalled here that the application of the transition detection algorithm was constrained to $7\ \% \leq x/c \leq 93\ \%$ (see Sec. III.A); therefore, transition locations at $x/c < 7\ \%$ are not shown in Fig. 17. At the corresponding angles-of-attack, however, turbulent separation – rather than laminar-turbulent transition – had the strongest impact on the boundary-layer evolution. The cyan rectangle in Fig. 17 indicates the approximate range of angles-of-attack at which a variation in the transition location has a fundamental influence on the aerodynamic performance of airfoils designed for the mid-span region of wind-turbine rotor blades [8,10,13].

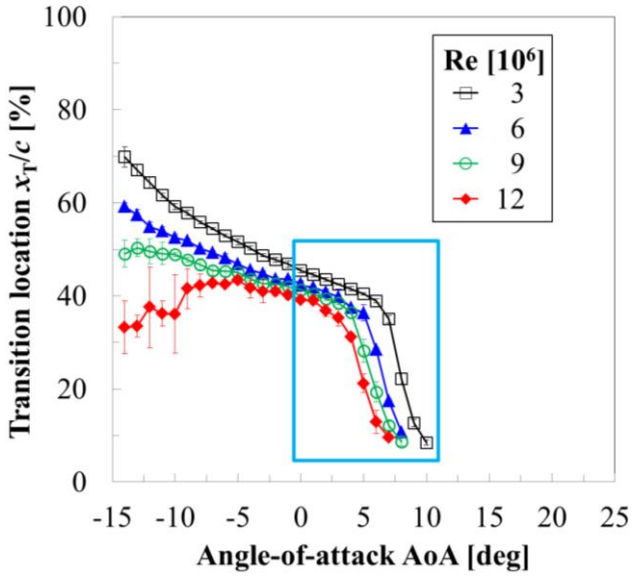

Fig. 17 Transition locations measured on the model upper surface at various angles-of-attack and Reynolds numbers.

For the reasons discussed in Sec. IV.B, transition on the model upper surface occurred at a more upstream location as the Reynolds number was increased. This finding was confirmed at all examined angles-of-attack. In general, transition was also shifted further upstream at larger angles-of-attack. Boundary-layer stability theory provided an explanation for this general trend – see Sec. IV.A.

The variation of the transition location as a function of the angle-of-attack can be subdivided into four sub-trends observed for different ranges of AoA, as presented below.

I) The first range of angles-of-attack considered here is $-14° \leq \text{AoA} \leq -6°$. At these negative angles-of-attack, an increase in AoA led to an upstream shift of the transition location for $\text{Re} = 3$ and $6 \cdot 10^6$. The variation in transition location from $x_T/c = 64.3$ % to 52.9 % shown in Fig. 3a-b (for an increase in angle-of-attack from AoA = -12° to -6° at $\text{Re} = 3 \cdot 10^6$) is representative for this sub-trend. As already mentioned in Sec. V.A, the evolution of x_T/c as a function of AoA observed at $\text{Re} = 12 \cdot 10^6$ was opposite to that at the two lowest Reynolds numbers: transition occurred at a more downstream location as the angle-of-attack was increased from AoA = -14° to -6°. In this range of angles-of-attack, at which transition occurred over a region of weak adverse pressure gradient, the larger turbulence level in the DNW-HDG test section at $\text{Re} = 12 \cdot 10^6$ may have led to a larger initial amplitude of the boundary-layer disturbances (see Sec. IV.B), thus inducing earlier transition. A stronger influence of the external disturbances on the boundary-layer instability and transition process may have led to the observed reduction in transition sensitivity to variations in the angle-of-attack

(i.e., in the streamwise pressure gradient). At $Re = 9 \cdot 10^6$, the evolution of the transition location with increasing AoA was generally similar to that observed at $Re = 3$ and $6 \cdot 10^6$, except for the increase in angle-of-attack from AoA = -14° to -13°. It is possible that, also at $Re = 9 \cdot 10^6$, the increase in turbulence level (as compared to the value of *Tu* at $Re = 3$ and $6 \cdot 10^6$) had a more important role in the boundary-layer instability and transition process at these weakest adverse pressure gradients. In fact, the evolution of the transition location with increasing angle-of-attack observed in [44] at $Re = 9 \cdot 10^6$ but for another combination of p_0 and U_∞ was in line with that found at $Re = 3$ and $6 \cdot 10^6$, i.e., transition was measured at a more downstream location at AoA = -14° than at AoA = -13°. This topic will be the focus of future work, where experiments will be conducted at various combinations of flow total pressure and freestream velocity for $Re = 9$ and $12 \cdot 10^6$.

II) A second sub-trend in the evolution of the transition location as a function of the angle-of-attack was observed at $-5° \leq AoA \leq AoA_{II}$, where the upper limit of the considered range (AoA_{II}) depended on the Reynolds number: it was $AoA_{II} = 3°$ at $Re = 12 \cdot 10^6$ and increased to $AoA_{II} = 6°$ at $Re = 3 \cdot 10^6$. In this range of angles-of-attack ($-5° \leq AoA \leq AoA_{II}$), the upstream shift of the transition location for a certain increase in AoA was smaller than that observed at $Re = 3$ and $6 \cdot 10^6$ in the first range of angles-of-attack ($-14° \leq AoA \leq -6°$). This different sensitivity of the transition location to changes in AoA was due to the stronger adverse pressure gradient inducing transition at $-5° \leq AoA \leq AoA_{II}$, as compared to the weak adverse pressure gradient at smaller angles-of-attack (see, e.g., Fig. 4). Moreover, the trend in the change of transition location as a function of AoA was similar for all examined Reynolds numbers: the gradients $\partial(x_T/c)/\partial AoA$ were in fair agreement in this range of angles-of-attack. The change in transition location from $x_T/c = 45.4$ % to 40.4 % presented in Fig. 3c-d (for an increase in angle-of-attack from AoA = 0° to 5° at $Re = 3 \cdot 10^6$) is representative for this sub-trend.

III) The gradient $\partial(x_T/c)/\partial AoA$ was then found to increase markedly at $AoA > AoA_{II}$, until the transition location reached the leading-edge region ($x_T/c < 7$ %, right end of the curves in Fig. 17). Representative for this third sub-trend are the TSP results in Fig. 3d-e, where a large upstream shift of the transition location was measured as the angle-of-attack was increased from AoA = 5° to 10°: from $x_T/c = 40.4$ % to 8.5 %. Also in this range of angles-of-attack, the evolution of the transition location as a function of the angle-of-attack was similar for all examined Reynolds numbers, with gradients $\partial(x_T/c)/\partial AoA$ in fair agreement. As compared to the previous range of angles-of-attack ($-5° \leq AoA \leq AoA_{II}$) the variation in pressure distribution on the model

upper surface with increasing angle-of-attack was more pronounced (see also Fig. 4); in particular, the adverse pressure gradient inducing transition started at a significantly more upstream location and became stronger at larger AoA.

IV) Once the transition location had reached the leading-edge region, a further increase in AoA led only to a small upstream shift of the transition location. This can be seen, for example, in Fig. 3e-g, where a large increase in the angle-of-attack from AoA = 10° to 20° led to a small variation in the transition location: from x_T/c = 8.5 % to a location just downstream of the leading edge. As can be seen in Fig. 4 for Re = $3 \cdot 10^6$, the start of the region of marked adverse pressure gradient was just downstream of the leading edge for all angles-of-attack in the range $10° \leq AoA \leq 20°$; the small difference in the transition location was only due to the magnitude of the adverse pressure gradient. Turbulent separation, rather than laminar-turbulent transition, became predominant for the boundary-layer evolution over the model upper surface at these large angles-of-attack.

C. N-factors at Transition

Transition N-factors on the model upper surface were determined for the examined test conditions according to the procedure described in Sec. IV. The obtained transition N-factors are presented in Fig. 18 as a function of the angle-of-attack. In this figure, symbols with different colors correspond to the values of N_T obtained at different Reynolds numbers. The average value of transition N-factor N_T = 8.4 (average of all presented data) is also indicated by a solid line. The corresponding standard deviation was $\Delta N_T = \pm 1.5$. As already discussed in Sec. IV, the reported transition N-factors should be taken with care, since most of the analyzed N-factor distributions were too steep for an adequate calibration of N_T. In this context, the cases with laminar separation predicted upstream of the measured transition location were particularly critical. Moreover, for the reasons discussed in Sec. IV.B, the values of N_T determined for Re = $12 \cdot 10^6$ at $AoA \leq -9°$ were not considered in the present analysis. At this largest Reynolds number, also at $-5° \leq AoA \leq 2°$ there are no available transition N-factors, since the resolution of the measured surface pressure distribution in the region of disturbance amplification appeared to be not suitable for the linear stability computations of these cases (see Sec. IV.B). These remarks must be well borne in mind while considering the following discussion.

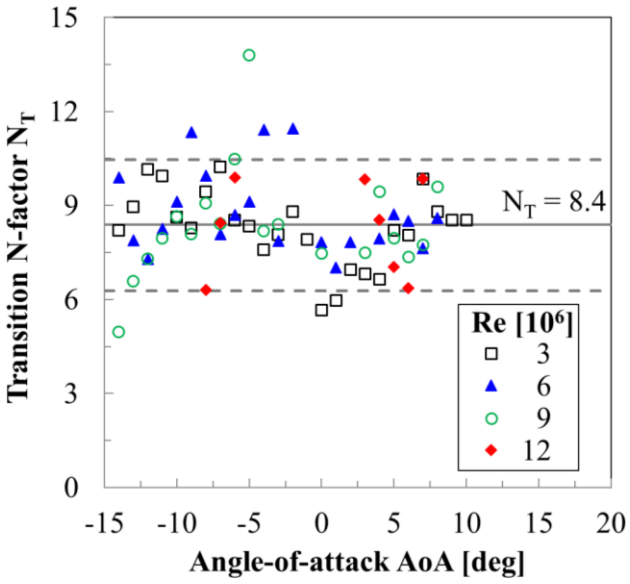

Fig. 18 Transition N-factors obtained at various angles-of-attack and Reynolds numbers.

The values of N_T presented in Fig. 18 show significant scatter. Most of the data, however, were within a band of ±25% around the average value of N_T – especially in the range of angles-of-attack corresponding to that highlighted in Fig. 17 by the cyan rectangle. This band is indicated in Fig. 18 by dashed lines. Such a variation of the transition N-factor is not uncommon and similar to that observed in other work, as for example in [33,36,51]. Note here that the average transition N-factors obtained at the different Reynolds numbers were in agreement, and that also the variations of N_T around the corresponding average values were similar for the four examined Reynolds numbers. Moreover, it should be emphasized that the average value over all analyzed data points, $N_T = 8.4$, was within the range of transition N-factors considered typical for quiet, low-turbulence wind tunnels ($8 \leq N_T \leq 10$) [45,48]. According to the commonly used Tu-N_T correlation formula from [52], the estimated turbulence level corresponding to $N_T = 8.4$ would be $Tu \sim 0.1$ %, i.e., even lower than the values reported in Sec. II. These observations on the transition N-factor and on the turbulence level appear to be a further confirmation that the adopted experimental setup (DNW-HDG wind tunnel and DU 91-W2-250 airfoil model equipped with TSP) was appropriate for the investigation of boundary-layer transition on airfoils designed for wind-turbine rotor blades.

VI. Conclusions

The aerodynamic performance of an airfoil designed for the mid-span region of modern wind-turbine rotor blades was experimentally investigated at large chord Reynolds numbers (up to $Re = 12 \cdot 10^6$) in the High-Pressure Wind Tunnel Göttingen, focusing on the laminar-turbulent transition on the airfoil upper side. The flow was subsonic: the freestream Mach number was below 0.1. Airfoil lift, drag, and pitching moment coefficients were obtained after integration of the pressure distributions measured on the surface and in the wake of the wind-tunnel model, whereas boundary-layer transition was measured globally and non-intrusively by means of the temperature-sensitive paint technique. The variation of transition location and aerodynamic coefficients was examined at four different Reynolds numbers ($Re = 3$, 6, 9, and $12 \cdot 10^6$) for a large range of angles-of-attack: from -14° to 20°. The measured surface pressure distributions served also as an input for boundary-layer computations, and the calculated boundary-layer velocity profiles were analyzed according to linear stability theory.

Boundary-layer transition was found to occur at a more upstream location as the Reynolds number was increased. This result was due to the upstream shift of the indifferent-stability point and to the enhanced amplification of Tollmien-Schlichting waves at larger Reynolds numbers, which led to earlier transition. In general, an increase in the angle-of-attack also led to a movement of transition into a more upstream location. Such evolution was due to the upstream shift and to the strengthening of the adverse pressure gradient inducing boundary-layer transition. This explanation was substantiated by the results of the boundary-layer stability computations, which showed an upstream movement of the indifferent-stability point and a more pronounced amplification of TS waves with increasing angle-of-attack.

At large angles-of-attack, the development of the boundary layer over the model upper surface was markedly influenced by turbulent flow separation. By means of the global TSP measurement technique, the separated flow region at stall and post-stall conditions was shown to be three-dimensional. The streamwise extent of the separated flow region and the spanwise distribution of the separation front were found to vary with increasing angle-of-attack and with increasing Reynolds number. The analysis of the TSP data also provided an explanation for the evolution of the lift, drag, and pitching moment coefficients measured at stall and post-stall conditions by means of the pressure sensors, which reported the local flow evolution in the region of the sensors but obviously could not capture the three-dimensional development of the boundary layer over the model surface. This observation clearly showed the

critical need for global measurements to be performed in combination with conventional pressure measurements, in order to correctly evaluate the aerodynamic performance of airfoils designed for wind-turbine rotor blades.

The measured transition locations were also correlated with the results of the boundary-layer stability computations, thus providing the amplification factors (N-factors) of Tollmien-Schlichting waves at transition. The average transition N-factor for the investigated airfoil model in the DNW-HDG wind tunnel was in the range of transition N-factors considered typical for quiet, low-turbulence facilities.

In conclusion, the present results demonstrated the importance of performing experiments on wind-turbine airfoils at large Reynolds numbers using a global measurement technique, such as TSP. The change in the flow evolution was shown to be significant, as compared to that at lower Reynolds numbers; its impact on rotor-blade performance has to be considered in the design phase and verified via experiments at Reynolds numbers relevant for modern wind turbines.

Acknowledgements

The authors would like to thank: Nora Falk and Stephan Hock (previously at DLR and TU Berlin) for the support to the TSP activities in DNW-HDG during their student projects; Tobias Kleindienst (DLR) and Ralf Lesjak (DNW) for the support during preparation of the wind-tunnel model; Melek Ekert (RWTH Aachen), Hitomi Sato and Naoya Tajima (Tohoku University) for the conduction and analysis of the TSP coating thickness and roughness measurements; and Günter Schewe (DLR) for the helpful discussions on the boundary-layer separation behavior of thick airfoil models at large angles-of-attack. The anonymous reviewers are also acknowledged for their valuable comments, which helped the authors to improve the quality of the manuscript.

References

[1] WindEurope, “Wind energy in Europe 2020. Statistics and the outlook for 2021-2025,” Brussels, 2021. https://windeurope.org/data-and-analysis/product/wind-energy-in-europe-in-2020-trends-and-statistics. [retrieved 15 Mar. 2021].

[2] European Wind Energy Association, “EU energy policy after 2020,” Brussels, 2011. http://www.ewea.org/fileadmin/files/library/publications/reports/EU_energy_policy_post_2020.pdf [retrieved 5 Jun. 2018].

[3] European Commission, “2030 Energy Strategy,” Brussels, Belgium, 2014. https://ec.europa.eu/energy/en/topics/energy-strategy-and-energy-union/2030-energy-strategy. [retrieved 5 Jun. 2018].

[4] WindEurope, "Wind energy in Europe: Scenarios for 2030," Brussels, Belgium, 2017. https://windeurope.org/wp-content/uploads/files/about-wind/reports/Wind-energy-in-Europe-Scenarios-for-2030.pdf. [retrieved 5 Jun. 2018].

[5] Naughton, J. W., "Instrumentation and Test Facility Needs for Wind Turbine Technology Development," AIAA Paper No. 2012-0697, 2012. doi: 10.2514/6.2012-697.

[6] Schaffarczyk, A. P., *Understanding Wind Power Technology: Theory, Deployment and Optimisation*, John Wiley & Sons, Chichester, UK, 2014. doi: 10.1002/9781118701492.

[7] Schaffarczyk, A. P., *Introduction to Wind Turbine Aerodynamics*, 2nd ed., Springer International Publishing, 2020. doi: 10.1007/978-3-642-36409-9.

[8] van Rooij, R. P. J. O. M., and Timmer, W. A., "Design of Airfoils for Wind Turbine Blades," GCEP Energy Workshop, Stanford University, 2004, 26 Apr. 2004.

[9] Schaffarczyk, A. P., Arakawa, C., "A thick aerodynamic profile with regions of negative lift slope and possible implications on profiles for wind turbine blades," Wind Energy, Vol. 24, 2021, pp. 162–173. doi: 10.1002/we.2565.

[10] Timmer, W. A., and Schaffarczyk, A. P., "The effect of roughness at high Reynolds numbers on the performance of DU 97-W-300Mod," Wind Energy, Vol. 7, No. 4, 2004, pp. 295–307. doi: 10.1002/we.136.

[11] Ehrmann, R. S., and White, E. B., "Influence of 2D Steps and Distributed Roughness on Transition on a NACA 63_3-418," AIAA Paper No. 2014-0170, 2014. doi: 10.2514/6.2014-0170.

[12] Schlichting, H., and Gersten, K., *Boundary-Layer Theory*, 8th ed., Springer–Verlag, Berlin, 2000.

[13] van Rooij, R. P. J. O. M., and Timmer, W. A., "Roughness Sensitivity Considerations for Thick Rotor Blade Airfoils," AIAA Paper No. 2003-0350, 2003. doi: 10.2514/6.2003-350.

[14] Rebstock, R., Zhai, J., and Schaffarczyk, A. P., "Experimental Investigation of Reynolds Number Effect on Wind Turbine Profiles in the Cryogenic Wind Tunnel Cologne DNW-KKK," Journal of Energy and Power Engineering, vol. 7, 2013, pp. 1957–1965. doi: 10.17265/1934-8975/2013.10.017.

[15] Schaffarczyk, A. P., Winkler, H., Freudenreich, K., Kaiser, K., and Rebstock, R., "Reynolds Number Effects on Thick Aerodynamic Profiles for Wind Turbines," Proc. European Wind Energy Conference and Exhibition, EWEA, Brussels, 2003.

[16] Viehweger, G., Rebstock, R., Stahl, B., Wichmann, K., Becker, W., Kronen, R., and Distelrath, D., "Der Kryo-Kanal Köln (KKK) der DLR (Stand 1992)," DLR-Mitt. 93-10, 1993.

[17] Klein, C., Henne, U., Sachs, W. E., Beifuss, U., Ondrus, V., Bruse, M., Lesjak, R., Löhr, M., Becher, A., and Zhai, J., "Combination of Temperature-Sensitive Paint (TSP) and Carbon Nanotubes (CNT) for Transition Detection," AIAA Paper No. 2015-1558, 2015. doi: 10.2514/6.2015-1558.

[18] NASA, "Low Turbulence Pressure Tunnel." https://crgis.ndc.nasa.gov/historic/Low_Turbulence_Pressure_Tunnel [retrieved 27 Sept. 2018]

[19] Försching, H., Melzer, E., and Schewe, G., "Ein neuer Windkanal für gebäudeaerodynamische und -aeroelastische Untersuchungen bei Reynoldszahlen bis 10^7," Konstruktiver Ingenieurbau, Vol. 35/36, 1981, pp. 127–133.

[20] Klein, C., Henne, U., Sachs, W. E., Beifuss, U., Ondrus, V., Bruse, M., Lesjak, R., and Löhr, M. "Application of Carbon Nanotubes (CNT) and Temperature-Sensitive Paint (TSP) for the Detection of Boundary Layer Transition," AIAA Paper No. 2014-1482, 2014. doi: 10.2514/6.2014-1482.

[21] Llorente, E., Gorostidi, A., Jacobs, M., Timmer, W. A., Munduate, X., and Pires, O., "Wind Tunnel Tests of Wind Turbine Airfoils at High Reynolds Numbers," Journal of Physics: Conference Series, Vol. 524, 2014, Article No. 012012. doi: 10.1088/1742-6596/524/1/012012.

[22] Pires, O., Munduate, X., Ceyhan, O., Jacobs, M., and Snel, H., "Analysis of high Reynolds numbers effects on a wind turbine airfoil using 2D wind tunnel test data," Journal of Physics: Conference Series, Vol. 753, 2016, Article No. 022047. doi: 10.1088/1742-6596/753/2/022047.

[23] Ceyhan Yilmaz, Ö., Pires, O., Munduate, M., Sorensen, N. N., Reichstein, T., Schaffarczyk, A. P., Diakakis, K., Papadakis, G., Daniele, E., Schwarz, M., Lutz, T., and Prieto, R., "Summary of the Blind Test Campaign to predict the High Reynolds number performance of DU00-W-210 airfoil," AIAA Paper No. 2017-0915, 2017. doi: 10.2514/6.2017-0915.

[24] van Hinsberg, N. P., Schewe, G., and Jacobs, M., "Experimental investigation on the combined effects of surface roughness and corner radius for square cylinders at high Reynolds numbers up to 10^7," Journal of Wind Engineering & Industrial Aerodynamics, Vol. 173, 2018, pp. 14–27. doi: 10.1016/j.jweia.2017.12.003.

[25] Madsen, H. A., Bak, C., Paulsen, U. S., Gaunaa, M., Fuglsang, P., Romblad, J., Olesen, N. A., Enevoldsen, P., Laursen, J., and Jensen, J., "The DAN-AERO MW Experiments," AIAA Paper No. 2010-0645, 2010. doi: 10.2514/6.2010-645.

[26] Reichstein, T., Schaffarczyk, A. P., Dollinger, C., Balaresque, N., Schülein, E., Jauch, C., and Fischer, A., "Investigation of Laminar–Turbulent Transition on a Rotating Wind-Turbine Blade of Multimegawatt Class with Thermography and Microphone Array," Energies, Vol. 12, No. 11, 2019, Article No. 2102. doi: 10.3390/en12112102.

[27] Schaffarczyk, A. P., Schwab, D., and Breuer, M., "Experimental detection of laminar-turbulent transition on a rotating wind turbine blade in the free atmosphere," Wind Energy, Vol. 20, No. 2, 2017, pp. 211–220.

[28] Quast, A., "Detection of Transition by Infrared Image Techniques," Technical Soaring, Vol. 30, No. 1/2, 2006.

[29] Fey, U., and Egami, Y., "Transition-Detection by Temperature-Sensitive Paint." In: Tropea, C., Yarin, A. L., and Foss, J. F. (eds.), *Springer Handbook of Experimental Fluid Mechanics*, Springer-Verlag, Berlin, 2007, Chap. 7.4. doi: 10.1007/978-3-540-30299-5.

[30] Liu, T., and Sullivan, J. P., Pressure and Temperature Sensitive Paint, Springer–Verlag, Berlin, 2005. doi: 10.1007/b137841.

[31] Mack, L. M., "Boundary-Layer Linear Stability Theory," Special Course on Stability and Transition in Laminar Flow, AGARD Rept. 709, Neuilly sur Seine, France, 1984, pp. 3-1 to 3-81.

[32] Costantini, M., Fuchs, C., Henne, U., Klein, C., Ondrus, V., Bruse, M., Löhr, M., and Jacobs, M., "Experimental Analysis of a Wind-Turbine Rotor Blade Airfoil by means of Temperature-Sensitive Paint," AIAA Paper No. 2019-0800, 2019. doi: 10.2514/6.2019-0800.

[33] Costantini, M., Fey, U., Henne, U., and Klein, C., "Nonadiabatic Surface Effects on Transition Measurements Using Temperature-Sensitive Paints," AIAA Journal, Vol. 53, No. 5, 2015, pp. 1172–1187. doi:10.2514/1.J053155.

[34] Goodman, K. Z., Lipford, W. E., and Watkins, A. N., "Boundary-Layer Detection at Cryogenic Conditions Using Temperature Sensitive Paint Coupled with a Carbon Nanotube Heating Layer," Sensors, Vol. 16, No. 12, 2016, Article No. 2062. doi: 10.3390/s16122062.

[35] Ondrus, V., Meier, R., Klein, C., Henne, U., Schäferling, M., and Beifuss, U., "Europium 1,3-di(thienyl)propane-1,3-diones with Outstanding Properties for Temperature Sensing," Sensors and Actuators A: Physical, Vol. 233, 2015, pp. 434–441. doi: 10.1016/j.sna.2015.07.023.

[36] Costantini, M., "Experimental analysis of geometric, pressure gradient and surface temperature effects on boundary-layer transition in compressible high Reynolds number flow," PhD Thesis, RWTH Aachen University, 2016. https://elib.dlr.de/117965/

[37] Amecke, J., "Direkte Berechnung von Wandinterferenzen und Wandadaption bei zweidimensionaler Strömung in Windkanälen mit geschlossenen Wänden." DFVLR Rep. FB 85-62, 1985.

[38] Fey, U., Egami, Y., and Klein, C., "Using CryoTSP as a Tool for Transition Detection and Instability Examination at High Reynolds Numbers. In: Tropea, C., Jakirlic, S., Heinemann, H.-J., Henke, R., and Hönlinger, H. (eds.), *New Results in Numerical and Experimental Fluid Mechanics VI, Notes on Numerical Fluid Mechanics and Multidisciplinary Design*, Vol. 96, Spinger-Verlag, Berlin Heidelberg, 2008, pp. 227–234. doi: 10.1007/978-3-540-74460-3.

[39] Costantini, M., Henne, U., Risius, S., Klein, C., "A Robust Method for Reliable Transition Detection in Temperature-Sensitive Paint Data," Aerospace Science and Technology, 2021, accepted for publication.

[40] Schewe, G., "Reynolds-number effects in flow around more-or-less bluff bodies," Journal of Wind Engineering and Industrial Aerodynamics, Vol. 89, 2001, pp. 1267–1289. doi: 10.1016/S0167-6105(01)00158-1.

[41] Miozzi, M., Capone, A., Klein, C., Costantini, M., "Incipient stall characterization from skin friction maps," International Journal of Numerical Methods for Heat & Fluid Flow, published online: https://doi.org/10.1108/HFF-10-2019-0733.

[42] Disotell, K. J., Nikoueeyan, P., Naughton, J. W., and Gregory, J. W., "Global surface pressure measurements of static and dynamic stall on a wind turbine airfoil at low Reynolds number," Experiments in Fluids, Vol. 57, 2016, Article No. 82. doi: 10.1007/s00348-016-2175-z.

[43] Miozzi, M., Capone, A., Costantini, M., Fratto, L., Klein, C., and Di Felice, F., "Skin friction and coherent structures within a laminar separation bubble," Experiments in Fluids, Vol. 60, 2019, Article No. 13. doi: 10.1007/s00348-018-2651-8.

[44] Costantini, M., Fuchs, C., Henne, U., Klein, C., Ondrus, V., Bruse, M., Löhr, M., and Jacobs, M., "A Reliable Experimental Methodology for the Study of Wind-Turbine Rotor Blade Aerodynamics," Journal of Physics: Conference Series, Vol. 1222, 2019, Article No. 012001. doi: 10.1088/1742-6596/1222/1/012001.

[45] Arnal, D., Casalis, G., and Houdeville, R., "Practical Transition Prediction Methods: Subsonic and Transonic Flows," AGARD Rept. RTO-EN-AVT-151, Neuilly sur Seine, France, 2009, pp. 7-1 to 7-34.

[46] Schrauf, G., "COCO—A Program to Compute Velocity and Temperature Profiles for Local and Nonlocal Stability Analysis of Compressible, Conical Boundary Layers with Suction," ZARM Technik Rept., Bremen, Germany, 1998.

[47] Schrauf, G., "LILO 2.1—User's Guide and Tutorial," GSSC TR 6, Bremen, Germany, 2006.

[48] Van Ingen, J. L., "The e^N Method for Transition Prediction. Historical Review of Work at TU Delft," AIAA Paper No. 2008-3830, 2008. doi: 10.2514/6.2008-3830.

[49] Küpper, A., Rohardt, C.-H., "Determination of the N_{TS}-factor for the DNW-NWB," 19. DGLR-Fach-Symposium der STAB, Munich, Germany, 4-5 Nov. 2014. https://elib.dlr.de/95445/.

[50] Crouch, J. D., Kosorygin, V.D., "Surface Step Effects on Boundary-Layer Transition Dominated by Tollmien–Schlichting Instability," AIAA Journal, Vol. 58, No. 7, 2020, pp. 2943-2950. doi: 10.2514/1.J058518.

[51] Schrauf, G., Perraud, J., Vitiello, D., and Lam, F., "Comparison of Boundary-Layer Transition Predictions Using Flight Test Data," Journal of Aircraft, Vol. 35, No. 6, 1998, pp. 891–897. doi: 10.2514/2.2409.

[52] Mack, L. M., "Transition and Laminar Instability," JPL Publication 77-15, California Institute of Technology, Pasadena, CA, 1977.